Epithermal clast coating inside the rock avalanche-debris flow deposits from Mount Meager Volcanic Complex, British Columbia (Canada)

The corrections made in this section will be reviewed and approved by a journal production editor.

Karine Bernard kbernard@opgc.univ-bpclermont.fr

Laboratoire Magmas et Volcans, Université Clermont Auvergne – CNRS - IRD, OPGC, Campus Universitaire des Cézeaux, 6 avenue Blaise Pascal, 63178 Aubière, France

Abstract

The observational and semi-quantitative sedimentological analyses of the lithofacies assemblage contribute to describe at different scales the breccia matrix along the sheared and transformed contact between rock avalanche deposits and trailing debris flow deposits emplaced by a large landslide at Mt. Meager volcano in British Columbia in 2010. An inverted cataclastic gradient of crushed breccias in a fluidized and mixed matrix implies a structurally controlled flow regime and rapid deposition. The coating matrix changed the initial polymodal distribution of the debris-flow lithofacies. Clast shape evolution helps to characterize the cataclastic sorting during transport and fluidized disaggregation. A plot of matrix percent against matrix/gravels helps to distinguish primary hot fracturing of about 61% from initial dilation and sheared fracturing involving ~22% matrix. Extensional disaggregation between 73 and 79% matrix is related to hydromagmatic fragmentation within an epithermal system. Clayey mineral assemblages identified by XRD patterns are related to colloidal aluminium gel, cataclastic shear bands, and quartz microstructures in epithermal breccia zones (pH = 2–3, 200–350 °C, <10–20 GPa).Microstructural analysis differentiates the inner rim of coated clasts from their border and the surrounding matrix in impact melt breccias. Sequential coating stages are inferred during the propagation of the shock wave with an oscillatory relative speed during the inter-seismic period. We differentiate: 1) shock faulting which contributes to the impacted quartz (10–35 GPa) in a devitrified matrix and pseudotachylite coating related to frictional melting at the margin of a conduit; 2) shock response (85 GPa) in epithermal vein with calcic spheroids, CO_2 dissociation, and basaltic melt (70–101 GPa, >1500 °C); and 3) the secondary fracturing with flash heating and pressure pulse during cavitation (ΔP ~ 10 GPa, >1000–1500 °C), which generates pockets of partial melting, quartz spheroids, and a roll-over effect for the inner rim of coated clasts. The formation of impact melt breccias and the debris flow are related to the slowing elastic impact wave with an oscillatory relative speed during the inter-seismic period along a proximal strike-slip fault.This study helps identify how the proximal rock avalanche transformed into a highly mobile debris flow, larger examples of which pose a hazard to the town of Pemberton, at a distance of 65 km from Mt. Meager.

Keywords: ~~v~~Volcanic avalanche transformations; ~~e~~Epithermal coating; ~~p~~Pseudotachylite; ~~s~~Sedimentology; ~~m~~Microstructures; ~~l~~Local kinematics

~~1.~~1 Introduction

Pseudotachylite with epithermal clast coatings are rarely studied in rock avalanche-debris flow deposits. This thin layer of melted rock is observed at the base of the volcanic avalanche deposits such as the Pichu Pichu landslide in Peru, the volcanic avalanche fault zone in French Massif Central (Legros et al., 2000; Bernard and van Wyk de Vries, 2017). This can be formed from frictional flash heating between the non-depositional and depositional emplacement. Several models consider specific conditions to generate frictionites along superfaults (≥1000–1500 °C, Spray, 1997, 1999a, 1999b; Magloughlin, 2005; Bestmann et al., 2011; Lavallee et al., 2012). These may be related to collapse, landslide and caldera formation. Microstructural investigations contribute to characterize matrix evolution of fault gouge from brecciation up to transformation such as rounded clasts surrounded by crushed material (~750 μm, Mount Saint Helens 2004–2006, Washington in the USA, Cashman et al., 2008) observed in the dacite spines. These lithofacies implicate hydrothermal fragmentation of conduit fault during lava dome extrusion. Disaggregation and sedimentary processes change the permeability and pore pressure along the discontinuities of a volcanic system (Farquharson et al., 2016).

Breccia zones must be considered to understand the clasts and matrix textures with hydrothermal alteration along fractures (Mount Rainier, Cascades Arc in the USA, John et al., 2008). The incorporation of clay can change flow dynamics: we differentiate the non-cohesive deposits (<3% silt + clay, Mount Saint Helens volcano, G1icken, 1986) and cohesive debris-flow deposits (>3% silt + clay, Mt. Rainier, Scott et al., 1995). Unconfined and water-saturated debris avalanche deposits commonly contain coated clasts attributable to matrix cementation and marginal lithofacies with >90% interclastic matrix rich in allophane (Palmer and Neall, 1991). Rock-avalanche transformations into debris flows result from impacts, disaggregation of megaclasts and of hydrothermally altered rock masses (1–4% clay, prehistoric Tahoma lahars, ~30 m/s), and reworking of finer grain-size fractions during transit by dilution and bulking (>3–5% clay; 1980 North Fork Toutle River debris flow from Mount Saint Helens volcano, Pierson and Scott, 1985; Scott et al., 1995, 2005). In the latter case, distal granular collisions generate frictional shear resistance.

Water-saturated collapses of hydrothermally altered volcanic deposits have been well documented in the Northern part of the Cascade volcanic belt (*i.e.*, Mount Rainier, Mount Saint Helens, Mount Meager, G1icken, 1986; Jordan, 1994; Scott et al., 1995, 2005; Vallance and Scott, 1997; Simpson et al., 2006; Friele et al., 2008; McKinnon, 2008; Guthrie et al., 2012; Roberti et al., 2017). In particular, the Mount Meager volcanic complex (Hickson et al., 1999) in southern British Columbia experiences frequent large rock and debris avalanches (10 to 25 events from 1850, including one with a volume of about 50 Mm^3 in 2010, magnitude = 2.6, Guthrie et al., 2012) that transform into large debris flows and hyperconcentrated floods that travel long distances from the source. The ratio of the vertical drop with runout distance (H/L) is around ~0.172. Incorporation of snow and glacier ices in the case of the Mt. Meager events leads to fluidization and

transformations of rock-avalanche deposits into high velocity debris flows. Simulations of the Mount Meager event (Hungr, 1995) using a dynamic analysis model, DAN-W, required a switch from a frictional to a Voellmy models to effectively account for frictional and turbulence characteristics (British Columbia, McKinnon, 2008; Guthrie et al., 2012). The two-dimensional numerical model, DAN-W, has been used to simulate run-out distance, velocity, the extent of deposition. More generally in such cases, desaturation of the pre-avalanche mass is followed by matrix mobilization (typically 75% sand and finer particles, Reid et al., 2001) and loss of fluids. Yet, even with this transformation, the structure and composition of the original rock mass may be preserved in the downstream deposits (Roberti et al., 2017). Pseudotachylite clast coatings are not described in rock avalanche-debris flow deposits. But a vitroclastic matrix is observed in the welding block-and-ash flow deposits, which filled the Lilloet River valley (bx2 units, Hickson et al., 1999; Michol et al., 2008; Russell et al., 2007; Andrews et al., 2014; Heap et al., 2014). These characterize the glass transition temperature of melt phase during the 2360 B.P. eruption of Mount Meager, similar to Soufriere Hills volcano (Montserrat).

In this paper, we document the sedimentary characteristics of clayey chondrules and coated clasts in outcrops at the sheared and washed contact between the rock-avalanche and debris flow deposits at Mount Meager volcano (6.08.2010, M 2.5 with v ~ 80 m/s, Guthrie et al., 2012; Roberti et al., 2017).

The aim of this study is to characterize the evolution of specific conditions during avalanche faulting and granular disaggregation generating proximal avalanche transformation into a debris flow surge.

~~2.~~2 Analytical methods

Analytical methods have involved field observations made between 2 and 9 October~~,~~ 2011 and sampling of the non-cohesive breccia matrix along the sheared contact between the 2010 Mt. Meager rock-avalanche and debris flow deposits. A semi-quantitative sedimentological analysis was conducted to determine grain size at different scales related to the microstructures of the coated clasts. From these data, we were able to establish the sedimentary characteristics of the transformed matrix associated with the clast coatings.

~~2.1.~~2.1 Outcrop-scale observations and sampling

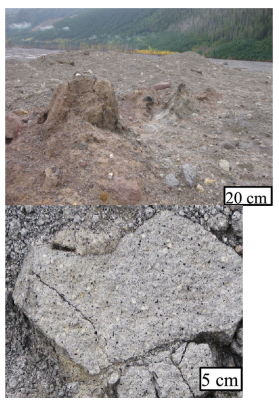
Sedimentary deposits and textural variations are described with internal structures of the different lithostratigraphic units (Table 1). Use of the Shape Preferred Orientation software (SPO, Launeau and Robin, 1996) provided a semi-quantitative description of breccia deposits, allowing us to estimate the a/b ratio (largest axis/minor axis), clast axial distributions and clast imbrications. Clast/matrix ratios in matrix deposits are calculated by binary image analysis using the software ImageJ (Bernard, 2015).

alt-text: Table 1

~~Table 1.~~Table 1

The table layout displayed in this section is not how it will appear in the final version. The representation below is solely purposed for providing corrections to the table. To preview the actual presentation of the table, please view the Proof.

Lithofacies and textures of deposits along the sheared contact between the 2010 Mt. Meager rock-avalanche deposits and debris flow. Structural units and the nomenclature lithofacies are referred to in Fig. 1.

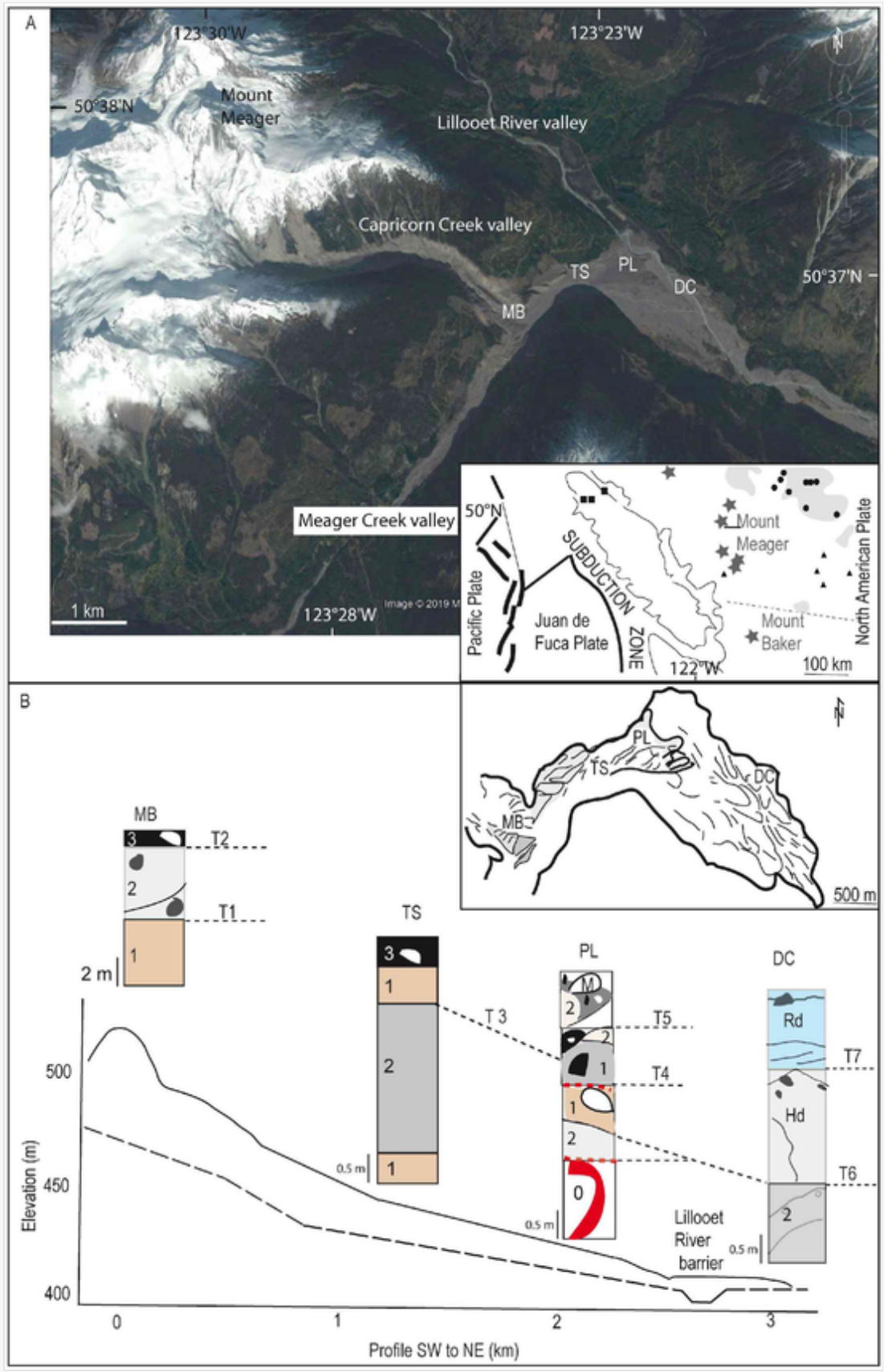
	Lithofacies and textures	Observed deposits
Mixed avalanche matrix	Different sandy-gravelly lithofacies in MB with a unimodal distribution between 12~~-~~ and 27% matrix. A brown clayey matrix (1 from G2, secondary peak failure in Figs. 1 and 2) related to epithermal alteration. Sliding of mixed rhyodacite breccias (2 from G1, first failure of the upper slope) with red blocks (2~~-~~–3 m). A mixed and transformed matrix with sub-rounded blocks (<50 cm) of rhyodacite (3).	
Reworked flow breccias	Different units in TS with gravel to sandy-gravel textures. Cataclastic flow breccias of grey rhyodacite in the diluted tail. Cataclastic rhyodacite breccias in hemi~~-~~horsts with jigsaw-fractures. A brown clayey matrix in graben is overlain by a matrix mixture showing chaotic surface of sub-rounded rhyodacite blocks reworked along the sheared contact. Reworked and transformed matrix breccias in the graben with alignment of thrust angular blocks ==>	
Avalanche thrust lobe	Different gravel units along serial thrust contacts in PL with unimodal distributions between 3 and 41% matrix. Thin discontinuous lithofacies along the back-thrust. Thrust and fold of matrix breccias with basal bulking. Underlying, water saturated lithofacies are extruded along reverse faults. ==> These lithofacies are associated with mesoscale structures (Figs. 2C and 3): flame structures, cataclastic injections of hydrothermalized brown lithofacies and matrix accommodation along shear bands. Frontal thrust with mixed matrix lithofacies reworked into debris-flow. Thrust of grey andesitic breccias with jigsaw breccias and crushed blocks. ==>	
Hybrid avalanche deposits~~-~~, debris-flow deposit	Polymodal hybrid avalanche deposit in DC with gravel to sandy gravel textures showing southeast rhyodacite blocks with N120 striations (S). ==> Eroded debris-flow deposit with bimodal to unimodal distributions.	

Forty-one non-cohesive samples of matrix were collected at the surface of the rock avalanche-debris flow deposits in the following structural units (Fig. 1A, Guthrie et al., 2012): thirteen samples from the debris barrier along the ridges at the Capricorn-Meager confluence (MB in Fig. 1A, 7 km, ~30~~-~~–50 m thick); six samples from the transport spray (TS) fault characterized by horst and graben structures; seven samples along the accretionary Plug Fold (PL, ~10~~-~~–15 m thick) at the Meager

Creek-Lillooet River secondary confluence; and twelve samples at the distal limit of the debris-avalanche deposit (DC), just downstream of where Lillooet River over-topped the deposit.

alt-text: Fig. 1

~~Fig. 1.~~Fig. 1



Geological setting of the 2010 rock avalanche-debris flow deposits from Mount Meager Volcanic Complex. A. From Google Earth, landforms and lithofacies of the rock avalanche-debris flow deposits sampled in each structural unit. Inset bottom right shows the location of the Cascade magmatic arc related to the subduction of Juan de Fuca plate. B. Profile of the structural units with simplified lithostratigraphic columns established from field observations. Inset top right shows the location of the four structural units (Guthrie et al., 2012): debris barrier along the ridges at the Capricorn-Meager confluence (MB), the Transport spray (TS) fault with horst and graben structures, the accretionary Plug Fold (PL) at the Meager Creek-Lillooet River confluence, and limit of the volcanic debris-avalanche deposit (DC). 1. Clayey brown matrix; 2. Cataclastic grey andesite; 3. White rhyodacite blocks in mixed lithofacies. Hd. Hybrid avalanche deposit; M. Mixed lithofacies; Rd. Reworked deposits into debris flow; T1-T7. Unconformity contacts. (For interpretation of the references to colour in this figure legend, the reader is referred to the web version of this article.)

~~2.2.~~2.2 Laboratory analysis

Complementary methods are used to characterize the grain-size distributions: 1. sieving of the coated clasts compared to dry sieving of the clasts and matrix at a one-Φ interval in the >~~-~~ ~~–~~ 5 to <5 Φ size; 2. Laser particle-size analysis (Malvern Master Size) of the finer particles (<32 μm, CNRS UMR 6296 in Clermont, France); 3. and the Fourier shape analysis using the ImageJ Plugin "Gold morph" to compute the maximum Feret diameter (Blott and Pye, 2008; Crawford and Mortensen, 2009). The cumulative curves of the grain-size distributions were compared to distinguish the matrix lithofacies in each structural unit. Grain-size distributions were processed using the Gradistat v8 software in Excel to compute the following statistical parameters: median diameter (*Md*), sorting index (σ), skewness (*SKG*) and kurtosis (*K*, Folk and Ward, 1957). The percentage of matrix (≤2 mm) and the matrix-gravel ratio help to identify the fragmentations related to the matrix transformations in each structural unit. Fractal dimensions of the size distributions were estimated with exponent *h* of the power regressions and fractal *D*-values (correlation coefficients between 0.9~~-~~ and 0.99, Suzuki-Kamata et al., 2009) correlated with range of clast sizes in millimeters. To gain insight into fragmentation and transport processes, Sequential Fragmentation Transport software (SFT, Wohletz et al., 1989) was used to subdivide the polymodal grain-size curves into subpopulations identified by dispersion γ(*g*) values such as magmatic (γ = −0.9 to −0.5) or hydromagmatic fragmentation (γ > −0.5), saltation (γ = −0.7 to 0.3), suspension (γ = −0.7 to 0.1), traction (~~-~~γ = −0.7 to −0.5) and ballistic (γ = −0.9 to −0.6).

~~2.3.~~2.3 Micro-scale analysis

Semi-quantitative microtextural analyses of thin sections contributed to differentiating the mineralogical assemblage of the inner and outer rims of clasts from the surrounding matrix. We examined the coating matrix of clasts in each structural unit using a binocular microscope on 108 clasts of thin sections ranging in size from 2 to 8 mm. The matrix percent and clast/matrix ratio in the coating matrix are calculated using the software ImageJ and SPO analysis (Launeau and Robin, 1996; Bernard, 2015). A Fourier shape analysis was applied to 430 clasts of thin sections to calculate the maximum Feret diameter, the axial ratio, the perimeter roughness, and the Riley circularity indices (Blott and Pye, 2008; Crawford and Mortensen, 2009; Bernard, 2015). We estimated qualitatively the relative abundance of minerals as a function of microtextural variations between the inner and outer rim of clasts. We provide information regarding mineral assemblages, microtextural differences of clast coatings, and shock deformed broken phenocrysts.

Quantitative X-ray diffraction analyses (XRD, X'Pert PRO of UCA-PARTNER-DRX in Clermont, Cu Kα1 radiation: $\lambda = 1.5405$ Å) were carried out on the clay-size (<2 μm) fraction of matrix samples following centrifugation of the suspended fines. The samples were air-dried, saturated in ethylene-glycol, and then heated at 400 °C for 40 ~~minutes~~min to identify hydrothermally altered assemblages. We used scanning electron microscopy with electron microprobe analysis (SEM, Jeol JSM-5910LV with X-ray Spectrometer, LMV) to differentiate the distributions of major elements in the coated and clayey clasts (312 analyses, in wt%, Table 3). The objective of this analysis was to relate microstructures such as cataclastic bands to frictional heating.

Detailed microscopic observations and SPO analysis of 2165 clasts characterized the micro-textures of the clast coatings and their relations to the granular distributions and a/b ratios (Launeau and Robin, 1996). Cumulative frequency was plotted against clast long-axis on double-logarithmic graphs and fractal dimensions h and D of size distributions were estimated from the power regressions (Suzuki-Kamata et al., 2009). Several statistical regressions have been established to characterize the kinematic processes involved in the proximal transformations of the rock avalanche into debris flow deposits.

~~3.~~3 Geological setting

The Cascade magmatic arc in western Canada is related to subduction of the Juan de Fuca plate beneath the North America plate (Fig. 1A, Hickson et al., 1999; Simpson et al., 2006; Friele et al., 2008). The Quaternary volcanic rocks in the Garibaldi belt are highly fractured and in part, hydrothermally altered, which contribute to unstable slopes on the deeply eroded and partially glacier-clad volcanoes (Read, 1979; Simpson et al., 2006; Friele et al., 2008). The 2360 B.P. eruption of Mount Meager produced the welded block and ash flow deposits that filled and dammed the Lilloet River valley (Michol et al., 2008; Andrews et al., 2014; Graham et al., 2014; Heap et al., 2014). An outburst flood resulted from the failure of a dam formed by welded block and ash flow deposits and produced a hot lahar (Hickson et al., 1999; Michol et al., 2008; Heap et al., 2014; Graham et al., 2014). The Mount Meager volcanic complex (MMVC, Hickson et al., 1999), which comprises about 20 km^3 of dacitic and rhyodacitic flows and pyroclastic rocks dating from about 2.2 *Ma* to 2400 ka, is the most unstable of these volcanoes (Read, 1977; Evans and Raffensperger, 1992; Clague et al., 1995; Hickson et al., 1999).

These rocks are highly fractured and dissected by faults, which provide paths for hydrothermal fluids and groundwater. Fumaroles that have formed ice caves are observed in Job Glacier on the north side of the MMVC (Roberti, 2019) and a hot spring is present in the valley of Meager Creek on the south side of the massif. In 2010, water-saturated rock avalanche deposits transformed into a high-velocity debris-flow (up to 80 m/s) that runout 12 km from the source into Lillooet River valley. The initial collapse of a mass of rhyodacite (G1, first failure of the upper slope) onto Capricorn Glacier destabilized the water-saturated and partly hydrothermally altered flank (G2, secondary peak failure) of Mount Meager, triggering the rock avalanche that fell into the head of Capricorn Creek valley and impacted the opposing valley wall (G3, the impact of the rock slide). The rock mass rapidly disintegrated and liquefied producing a debris flow surge that bulked about 30% (6 Mm^3, Guthrie et al., 2012). Temperatures within the massif are high (>200--300 °C, Read, 1979; Friele and Clague, 2004) at shallow depths. A fluidized outburst following the avalanche dam break-out (19 h, ~30--50 m thick, 700~~X~~×500 m at the base of the landslide dam, Guthrie et al., 2012) produced high velocity debris flows with long runout distances. The occurrence of similar events represents a hazard for Pemberton, at a distance of 65 km (Friele et al., 2008).

The studied outcrops exhibit an inherited sheared and washed contact between the inertial granular mass flow of the avalanche deposits and the eroded outburst flood (Guthrie et al., 2012; Roberti et al., 2017). Field observations and semi-quantitative analysis have been used to identify the sedimentary characteristics of the impact wave transformations related to the *syn*-transport kinematic transition from non-depositional to depositional flow conditions along the sheared and transformed interface.

~~4.~~4 Results

~~4.1.~~4.1 Lithofacies variations along fault zones

Deposit morphology and structures related to stratigraphy and textural observations of the discontinuous lithofacies assemblage contribute to differentiating structural units of the rock avalanche-debris flow deposits (Fig. 1A, Guthrie et al., 2012; Roberti et al., 2017). The debris barrier exposes compressional ridges of mixed debris along basal thrust contact at the Capricorn-Meager confluence (MB, 7 km, ~30--50 m thick, Fig. 1A). The transport spray (TS) fault is characterized by horst and graben structures eroded by the outburst flood. The accretionary Plug Fold (PL, ~1200 m long, ~10--15 m thick; Roberti et al., 2017) with triangular shape exhibits thrusts and strike-slip-faults at the Meager Creek-Lillooet River secondary confluence. Serial sheared contacts (T1-T7) are differentiated from MB to DC (Fig. 1B). The blocks and mixed deposits are overwhelmed by the dam-breach flood (Guthrie et al., 2012; Roberti et al., 2017). The distal limit of the debris-avalanche deposit (DC), just downstream of where Lillooet River over-topped the deposit, consists of hummocks, compressional ridges and orientated blocks (<100 m, Mehl and Schmincke, 1999).

We differentiate metric-size blocks exposed in MB and DC, crushed megaclasts and clasts dispersed in different matrix lithofacies. The isolated blocks are mainly composed of rhyodacite or dacite. Dihedral blocks in MB are impacted in the gravel-sized matrix. We observe abraded, planar surfaces with striations (Table 1). These are surrounded by angular clasts of rhyodacite and overlain by different matrix-rich lithofacies.

We observe a brown clayey matrix (1), which is overlain unconformably (T1--2 in Fig. 1B) by a cataclastic, grey rhyodacite lithofacies (2) and a matrix-rich lithofacies (3, Fig. 1B) showing sub-rounded rhyodacite blocks. A semi-quantitative description of deposits is established using a SPO analysis of the 1157 clasts and the software ImageJ (see Supplemental File 1). The clast/matrix values are between 0.54 in MB and 1.09 in DC with a mean value around ~0.93. The mixed debris in MB is associated with a polymodal clast-size distribution, with $a/b = 1.35$ and ellipse = 3.87 (SPO from 51 clasts, Table 1). We differentiate the cataclastic, grey rhyodacite lithofacies (2) in downstream of the Capricorn-Meager confluence (Fig. 2A). The flow breccias are extruded and tilted northward. Cataclastic lava

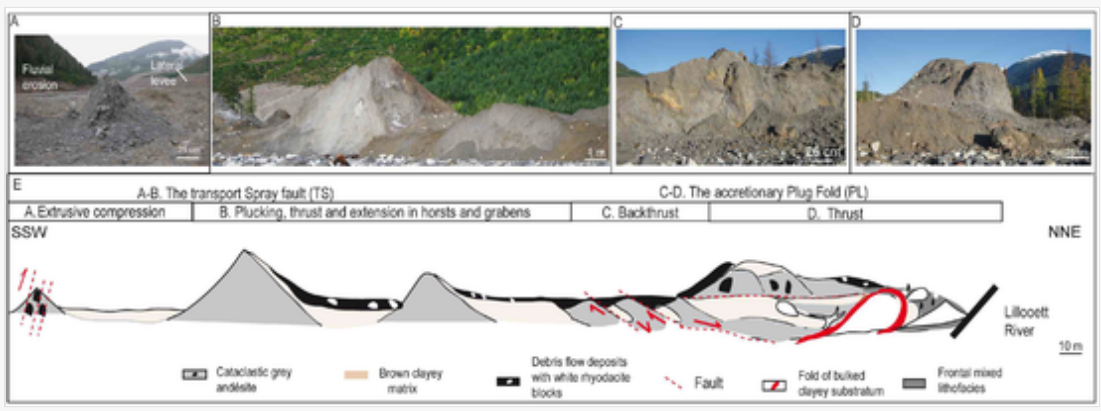
breccias are tilted in semi-horsts and matrix mixture in graben in downstream of frontal thrust (Fig. 2B). Jigsaw fractures are observed in the cataclastic rhyodacite breccias in semi-horsts (Fig. 2B). The grabens are filled by a brown clayey matrix (1) overlain by a mixed matrix (3 in Fig. 1, Table 1). The clast-size distribution is unimodal with mean values around a/b = 1.13 and ellipse = 15.2 (SPO from 193 clasts, see Supplemental File 1).

Along the extensional faults, the rhyodacite breccias are tilted and sheared (Fig. 2B). At the confluence, the frontal deposits have been back-thrust (Fig. 2C). Cataclastic lava breccias in semi-horst and matrix mixture are thrust with unconformity contacts at the front lobe (Fig. 2C–D). These are tilted and abraded along sheared contact. The thin discontinuous lithofacies are sheared along the inverted extensional faults. The thrust lobe (Fig. 2) is characterized by a series of thrust units at the front. The avalanche lithofacies assemblage becomes thicker along serial thrust contacts (Fig. 2D–E). A unimodal clast-size distribution characterizes the matrix deposits with mean values around a/b = 1.08 and ellipse = 8.32 (SPO from 749 clasts, see Supplemental File 1). Underlying, water saturated lithofacies (Figs. 2C and 3C–D, Table 1) are extruded along reverse faults. Debris-flow deposits and hybrid avalanche deposits are differentiated at the front of the thrust lobe. Locally, reworked alluvial pebbles are observed. The dam-breach flood has contributed to the polymodal clast-size distribution (SPO from 164 clasts) of the hybrid avalanche deposits with mean values around a/b = 1.08 and ellipse = 12.08. Clastic gradation of sedimentary lithofacies assemblage with reverse grading is correlated with deposit morphology (Figs. 1 and 2).

Mesoscale structures, that are about several ten in centimeters in width and up to 3 m in high, are observed inside frontal, thrust deposits into the dammed Lillooet River valley (PL in Figs. 2 and 3A). We observe cataclastic extrusion with extensional fractures and basal jigsaw fractures (Fig. 3B). Granular readjustments are localized in the mass-flow deposit: flame structures, cataclastic injections along reverse faults (Fig. 3B–C) and matrix accommodation along bands. Thrust and folds of matrix breccias are observed at the front of the thrust unit (Fig. 3D). At the confluence of the frontal lobe, the mixed lithofacies (~2–3 m thick, Fig. 3E) is overlain by debris-flow deposits characterized by a chaotic and abraded surface of extruded and tilted rhyodacite blocks. Southeast rhyodacite blocks with abraded surfaces and N120 striations (Table 1) are rafted in matrix breccia deposit incised in the Lillooet River valley. We observe laterally relict and eroded debris-flow deposits in DC (Figs. 1–2).

alt-text: Fig. 2

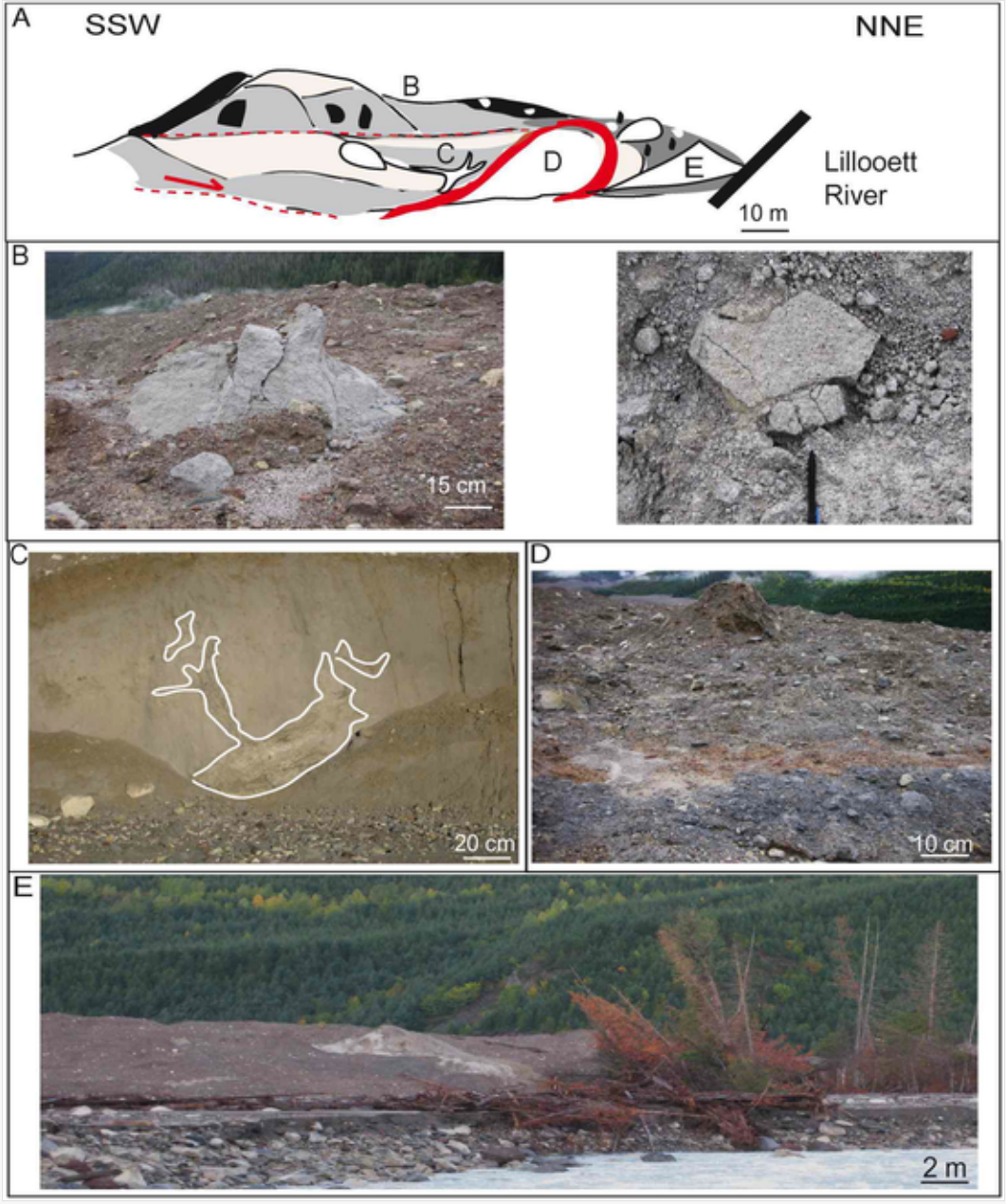
~~Fig. 2.~~Fig. 2



Structural gradation of lithofacies related to structures from 2 km runout distance. A. The flow breccias with extrusive compression and crushed blocks along reverse faults; B. Plucking, thrust, and extension in horsts and grabens; C. Back-thrust with reverse faults and flame structures; D. Thrust with shear bands. E. Structural units with different zones. Structural units and these nomenclature lithofacies are referred to in Fig. 1.

alt-text: Fig. 3

~~Fig. 3.~~Fig. 3



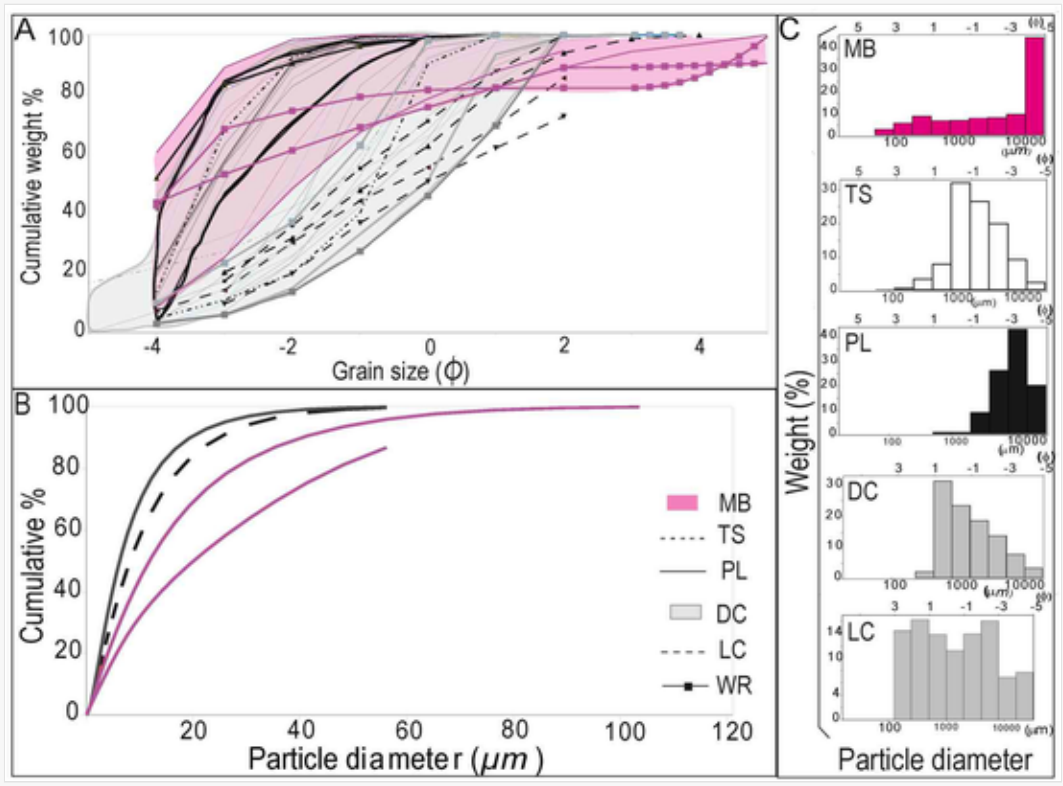
Mesoscale structures observed along the accretionary Plug Fold. A. The accretionary Plug Fold with different zones. B. Jigsaw fractures of lava blocks; C. Basal cataclastic injections; D. Bulking, thrust and folds in parallel bands of matrix breccias; E. Frontal thrust with mixed lithofacies and dilution downstream. Structural units and these nomenclature lithofacies are referred to in Fig. 1.

~~4.2.~~4.2 Sedimentary characteristics of the matrix breccias

To characterize the matrix breccias, forty-one non-cohesive samples of matrix were collected at the surface of the rock avalanche-debris flow deposits in the structural units. The comparison of each grain-size fractions with cumulative curves and histograms (Fig. 4) helps to differentiate the matrix sampled in each structural unit. The values of the gravel and sand fractions tend towards similar grain-size distributions between ~~-~~4 and +1 Φ. We recognize the sandy-gravel texture of the unimodal deposits, which are poorly sorted in MB (*Mz* ~~-~~ 2.59 Φ); the unimodal gravel deposits (*Mz* ~~-~~ 3.32 Φ), which are poorly to moderately sorted in PL; and gravel to sandy gravel texture in TS and DC (*Mz* ~~-~~ 2.1 Φ). Laser diffraction analysis (Fig. 4B) shows unimodal fine-grained to medium silts, including 60% of fractions around ~10 µm. The fine-grained matrix facies decreases in size from 28~~-~~ to 11 µm in MB to 13~~-~~6 µm in DC. The poorly sorted debris-flow deposits present bimodal to unimodal distributions, with 89% of samples having mesokurtic distributions (*K* from 0.9 to 1.11; Table 2). The hybrid avalanche deposits in DC are characterized by polymodal grain-size distributions (43% of samples, Bernard, 2015). The polymodal coarse sand fractions are related to platykutic distribution of deposits in each structural unit (*K* ~ 0.67~~-~~0.9, Fig. 4C, Table 2).

alt-text: Fig. 4

~~Fig. 4.~~Fig. 4



Sedimentological results from sieved samples of Meager deposits. A. Cumulative curves of the matrix between -5 and 5 Φ; B. Cumulative curves of fine-grained matrix (<63 μm) from laser diffraction analyses; C. Histograms. LC. Clast; WR. Whole particle range. Structural units and these nomenclature lithofacies are referred to in Fig. 1.

alt-text: Table 2

~~Table 2.~~Table 2

The table layout displayed in this section is not how it will appear in the final version. The representation below is solely purposed for providing corrections to the table. To preview the actual presentation of the table, please view the Proof.

Grain size parameters from sieved samples of the 2010 Meager rock avalanche-debris flow deposits: 1. Median diameter (*Md*); 2. Matrix percent; 3. Matrix/gravels; 4. Sorting index (σ); 5. Skewness (*SKG*); 6. Kurtosis (*K*, Folk and Ward, 1957); 7–9. Fractal analysis with exponent *h* of the power regression and fractal *D* values (correlation coefficients between 0.9 and 0.99, Suzuki-Kamata et al., 2009) correlated with range of clast sizes in millimeters; 10. Dispersion γ(*g*) values (Wohletz et al., 1989); 11. Travel distance in meters. Structural units and these nomenclature lithofacies are referred to in Fig. 1.

	1 *Md* (Φ)	2 *Matrix* %	3 *Matrix/gravels*	4 σ	5 SK_G	6 *K*	7 *h*	8 *D*	9 Range of clast sizes (*mm*)	10 γ(*g*)	11 Distance (m)
MB	–4.25–4.3	0–32.5	0–0.48	0,74–3.04	–0.86–0.64	0.81–4.43	0.03–2.29	–1.58–2.94	0.12 to 16	–0.92 + 5	0
Mean values	–2.55	11.72	0.17	1.34	0.09	1.29	1.01	0.97	0.12–16	0.28	
TS	–3.65-1.3	0–43	0–0.75	0.78–1.47	–0.33 + 0.04	0.84 + 1.11	0.34 + 1.54	–0.08 + 2.32	0.25–16	–0.81 + 3.98	
Mean values	–2.05	27.13	0.33	1.18	–0.14	0.94	0.87	1.24	0.25–16	0.6	
PL	–3.85–2.9	0–10.3	0 + 0.11	0.88–1.13	0 + 0.29	0.82 + 1.16	1.15 + 2.21	–1.42 + 0.7	0.5 to 16	–0.68 + 0.14	10,000
Mean values	–3.45	2.91	0.03	0.99	0.1	1.03	1.73	–0.43	0.5 to 16	–0.35	
DC	–1.75–1.35	17–66.9	0.2–1.35	1.1–2.58	–0.35–0.01	0.67–1	0.2–0.45	2.1–2.6	0.5 to 32	–0.91–0.19	>10,000
Mean Values	–1.36	40.89	0.89	1.45	–0.16	0.9	0.28	2.43	0.5–32	–0.47	

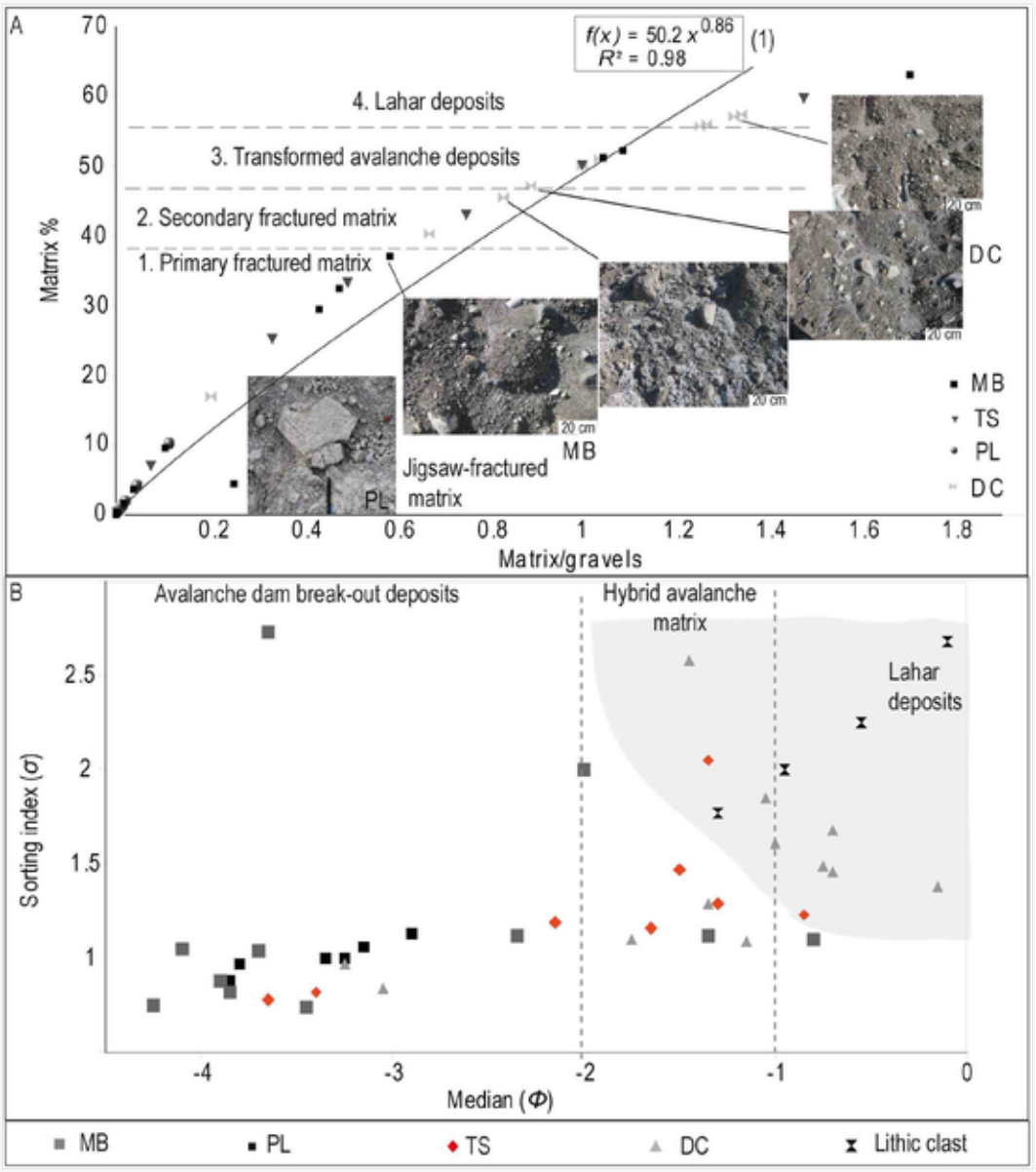
All the matrix samples present coated clasts (8–2 mm in diameter) and clayey chondrules (4–1 mm in diameter). The coating matrix of clasts changes the initial granulometric distribution by increasing the clast size and aggregating clay fraction. The coarse fraction (16 mm) is not observed in MB. The coating matrix in PL increases from 3.4 to 19% for the 2–8 mm size fractions, whereas the 0.5–1 mm size fractions decrease to 10%. The finer grain-size fraction is absent in the coating matrix. In the distal zone (DC), the <0.5 mm size fraction decreases from 39% to 14%, together with a concomitant increase in the 0.5–16 mm size fractions (from 23% for 16 mm size fraction to 5% for 2 mm size fraction).

The matrix percent *vs*. matrix/gravels diagram shows a power regression of the rock avalanche-debris flow deposits (Eq. (1) with $R^2 = 0.98$ in Fig. 5A). These values of the matrix samples are close to those of the discontinuous sandy layer before impact-sheared contact along avalanche fault zone in French Massif Central (Bernard and van Wyk de Vries, 2017). Along the runout distance (Table 2), the percentage of matrix increases from 12 to 27% in MB, from 3 to 41% in PL. The lateral deposits in MB contain about ~4.5% matrix and 0.25 matrix-gravel ratio. This power regression (Eq. (1) with $R^2 = 0.98$ in Fig. 5A) correlates all textural variations in mesoscale structures from a jigsaw-fit texture (~10 ~~centimeters~~cm in high) with <10% matrix to cataclastic breccias with 0.04–0.11 matrix/gravels in

PL and DC. The primary fractured matrix with <40% matrix and 0.37 to 0.55 matrix-gravel ratio occurs in MB and TS (1 in Fig. 5A). The thrust deposits in TS and DC contain 40–50% *syn*-emplacement breccia matrix and 0.66 to 0.9 matrix/gravels (2, Fig. 5A), due to the secondary fracturing. The secondary hybrid avalanche deposits in DC contain >50% matrix and a sand-sized matrix-gravel ratio >1 associated to the matrix transformations into lahar deposits.

alt-text: Fig. 5

~~Fig. 5.~~Fig. 5



Statistical parameters from sieved samples in different structural units of the Meager rock avalanche-debris flow deposits. A. Matrix % *vs*. matrix/gravels related to textural observations of lithofacies from MB to DC; B. Sorting index (σ) *vs*. median diameter (*Md*). Structural units and these nomenclature lithofacies are referred to in Fig. 1.

The dispersion γ(*g*) values of seven sub-populations (Table 2, Wohletz et al., 1989; Bernard, 2015) help to distinguish fragmentation and transport processes. Five sub-populations with mixed processes have been identified. The sandy grain-size fractions (>1 Φ) present 50% with magmatic fragmentation (γ =–0.79), and 50% with hydrovolcanic fragmentation (γ = 0.69). The matrix samples with *Md* <–1 Φ suggest an avalanche dam break-out origin (~68% sub-populations, Capra and Macías, 2002). We differentiate the medium sandy fractions (>0 Φ; γ =–0.48-0.69) suggesting a magmatic fragmentation and transport by traction in TS, and the coarser sandy fractions (<–1 Φ; γ ≥–0.48) with a hydrovolcanic origin and transport by saltation and suspension. The mean fractal *D*-value of matrix lithofacies (Table 2, Suzuki-Kamata et al., 2009; Bernard, 2015) is around ~1.95 in the 2–8 mm clast-size range. The fractal *D*-values of faceted, lithic clasts showing a shiny surface, increase from ~2.15 in MB to ~2.44 in DC. The fractal *D*-values of coated clasts range from 1.24 in the 0.25–16 mm clast-size range for the flow breccias along the horsts and grabens (TS), to 2.43 in the 0.25–16 mm clast-size range related to the secondary hybrid avalanche deposits in DC (Table 2).

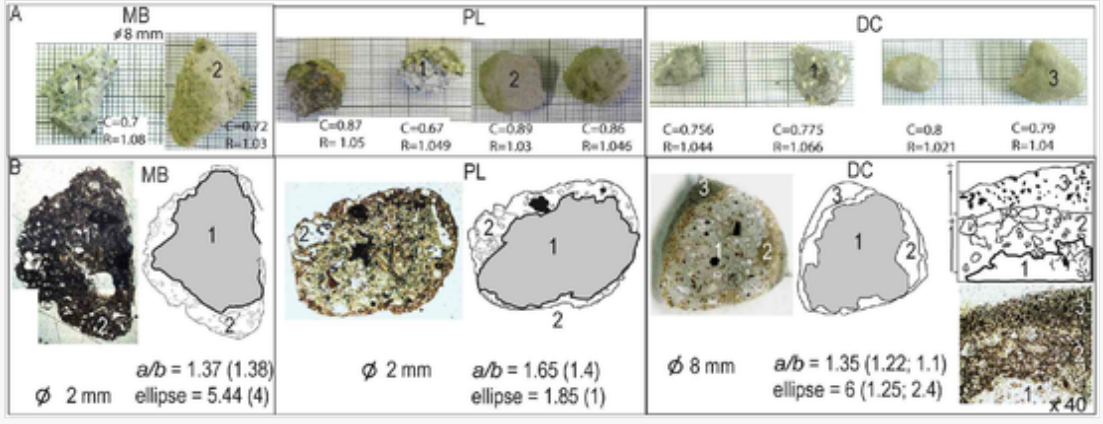
Statistical grain-size parameters highlight the internal processes of rock-avalanche transformations into debris-flow deposits. The sorting index (σ) *vs*. median (*Md*) diagram (Fig. 5B) helps to distinguish the avalanche dam-breakout deposits (σ <1.5, *Md* <–1 Φ, Capra, 2007), the secondary hybrid avalanche deposits (*Md* =–2-1 Φ) and the distal transformations into debris-flow deposits, which have similar values to the Pinatubo lahars (*Md* >–1 Φ, σ ~2.2, Table 2, Major et al., 1995) with 34% of samples including lithic clasts. Very platykurtic to platykurtic distributions (*SKg* from 0.1 to –0.16, Table 2) characterize the avalanche deposits transformed into non-cohesive debris-flow deposits. Skewness and kurtosis values decrease from MB to PL (*SKg* ~0.09 to –0.1, *K* ~1.2 to 0.9, Table 2), while the fractal *D*-values increase from 0.9 in MB to 1.2 in TS and –0.43 in PL to 2.43 in DC. The coarse skewness (>0.1) characterize the thrust deposits at the confluence (MB and PL).

~~4.3.~~4.3 Clast shape parameters of coated clasts

Binocular and microscopic observations are used to establish the textural and structural variations between the inner and outer rims of clasts in each structural unit (Fig. 6A). We calculate the evolution of the granular ratios and the clast shape parameters with the software ImageJ and the SPO analysis. The axial a/*b* ratios are between 1.1- and 1.4 for faceted clasts with a shiny surface and 1.35 to 1.65 for the coated clasts with ellipse values between 1 and 4. The ellipse/*a*/*b* values are between 4.05 and 1.02. Along the runout distance, the axial ratios increase (+0.29) in MB related to the coating matrix, and decrease downstream (–0.3 in PL) with the perimeter roughness (–0.78).

alt-text: Fig. 6

~~Fig. 6.~~Fig. 6



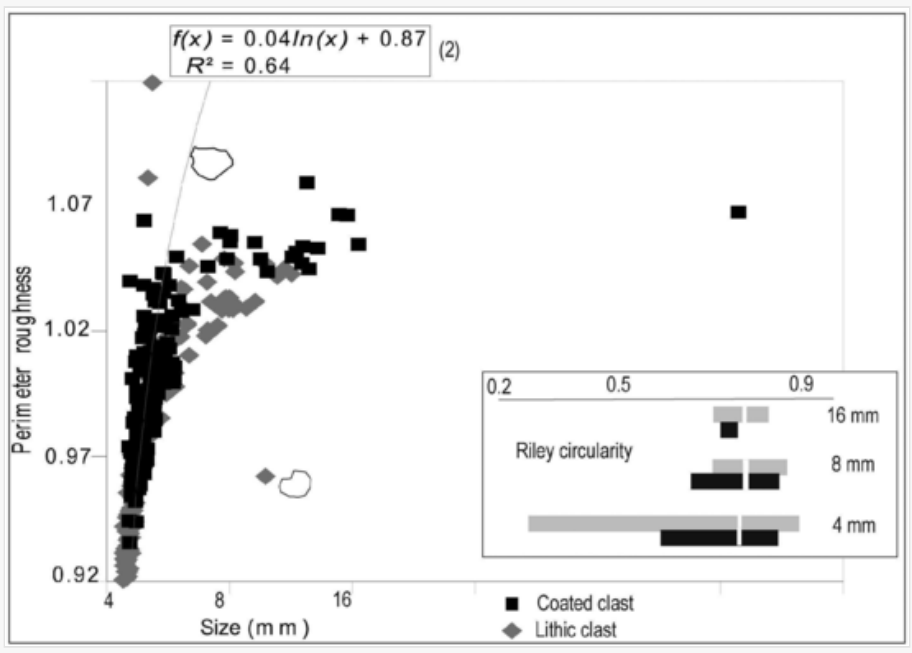
Coated clasts in each structural unit. A. Observations using binocular microscope with clast shape analysis (C: Riley Circularity; R: Perimeter roughness). B. Binocular microphotographs with SPO analysis (a/b, ellipse, Launeau and Robin, 1996) of coating matrix showing dacite clasts (1) with the inner (2) and outer (3) rims with reverse grading in DC; These nomenclature lithofacies are referred to in Fig. 1.

Microscopic observations show a microtextural gradient inside clastic coating (Fig. 6B). We differentiate the dacite clast (1, 80% of the volume) with sharp contours without hydrothermal alteration from the inner (2) and outer rims (3) with reverse grading. The clast coating appears irregular. We observe the occurrence of phenocrysts in the devitrified brown matrix. The inner rim diameters are between 0.1 ~~to~~ and 0.5 mm (~5 to 25% of volume, Fig. 4B) in MB and PL up to 1 mm in DC (12.5% of volume). The outer rim diameters in DC are between 0.1 ~~to~~ and 1 mm. The embayment boundaries increase the inner roughness of dacite clasts with a decreasing a/b ratio around ~1.22 in DC related to strong shearing within the clastic flux.

A logarithmic regression (Eq. (2) in Fig. 7) characterizes the increasing perimeter roughness *vs*. clast size. The perimeter roughness is high (~0.9 ~~-~~ 1) to compare the Riley circularity (~0.7). The variations of the perimeter roughness increase from 1 to 1.6 between MB to PL up to 2.9 in DC. With the runout distance, the variations of Riley circularity of the coated clasts decrease (~~-~~0.02) to compare the clasts (+0.08).

alt-text: Fig. 7

~~Fig. 7.~~Fig. 7



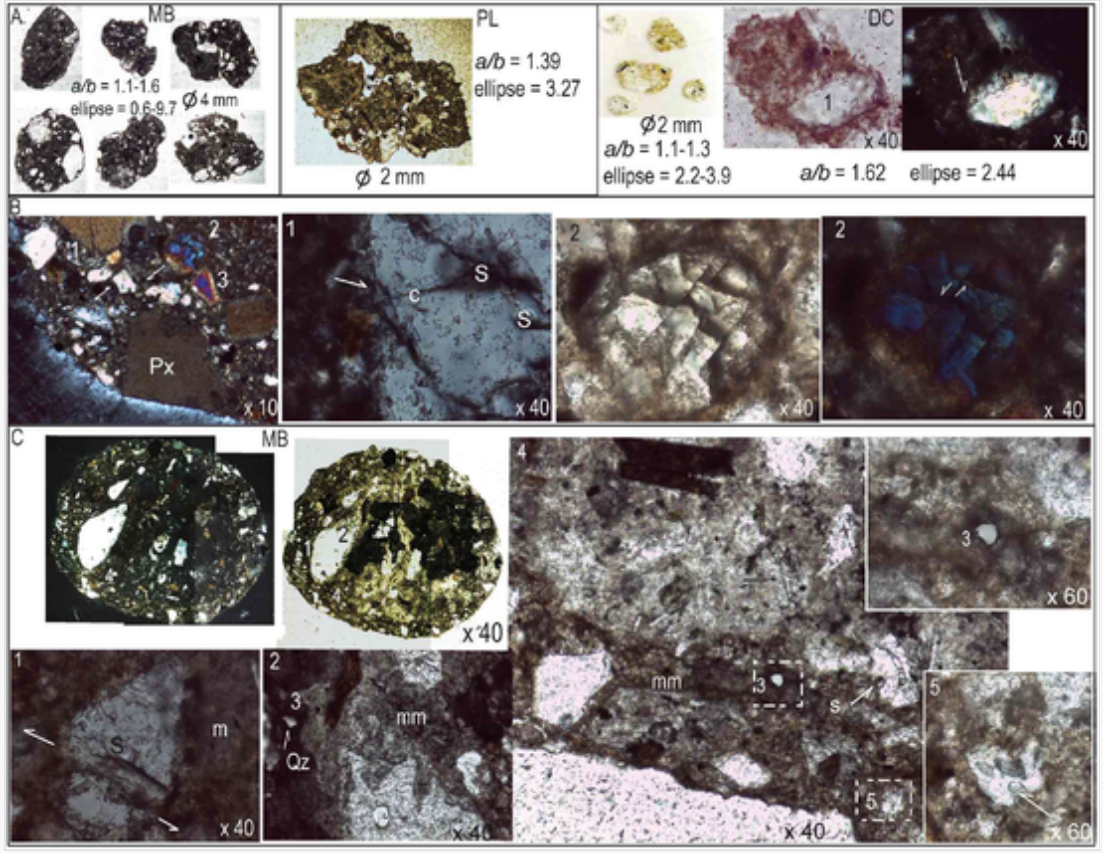
Perimeter roughness and Riley circularity *vs*. clast size (mm).

~~4.4.~~4.4 Microstructures of clayey chondrules

The clayey chondrules (1 ~~-~~ 4 mm in diameter, ellipse/a/b = 2.76, Fig. 8A) are composed of sub-angular phenocrysts of hydroclastic quartz and feldspars with a few biotite flakes and pyroxene in a devitrified brown matrix. From SPO analysis of twenty clayey chondrules in thirteen thin sections, we observe a shape evolution with strong variations of ellipse/a/b values between 0.5 and 6 from MB to PL, and similar values in DC (ellipse/a/b = 2 ~~-~~ 3).

alt-text: Fig. 8

~~Fig. 8.~~Fig. 8



Microstructures in clayey chondrules. A. Transmitted light microphotographs of clayey chondrules with SPO analysis showing shape evolution related to clastic matrix in each structural unit. We differentiate hydroclastic quartz (1 in DC) in devitrified matrix with impacted and recrystallized rim (*white arrow*) and fluid inclusions. B. Along sheared contacts within clayey chondrules, a linear flow texture (*white arrows*) of quartz microsclasts with heterogeneous extinction; partial isotropization along clast margins (3); black areas are microcracks (c) and cavitary fractures (S) in quartz (1) with impacted margins (*white arrow*) and fluid inclusions; sub-rounded quartz (2) with anomalous birefringence of kink bands along sheared planar fractures (*white arrows*) and partial isotropization with sub-parallel lamellae. C. In clayey chondrule, sinistral shear (1) of sub-angular feldspar phenocryst with cavitary fractures (S) in devitrified brown matrix (m); clast interactions (2) along crushed and sheared contact generating clastic matrix mixture (mm) with recrystallized asymmetric tridymite (3) in devitrified brown matrix; cataclastic shear bands (4). Insets show the enlarged areas of asymmetric deformations of quartz spheroids and cavities of quartz dehydration (5, *white arrow*) in matrix mixture (mm). c: microcracks; m: devitrified brown matrix; mm: clastic matrix mixture; Px: augite; Qz: quartz; S: cavitary fractures. (For interpretation of the references to colour in this figure legend, the reader is referred to the web version of this article.)

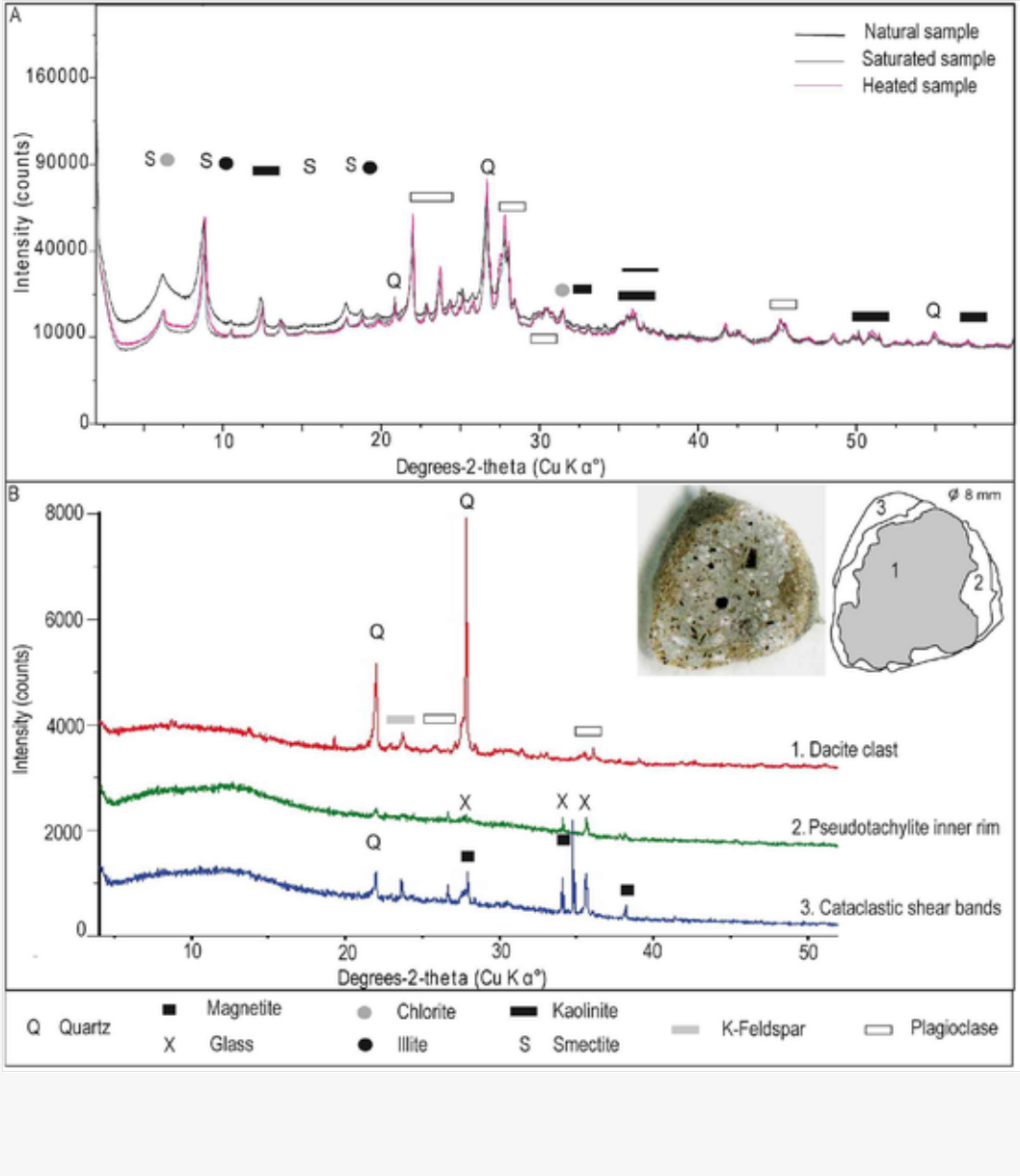
Linear flow textures along sheared contacts are observed in clayey chondrules (Fig. 8B). Quartz microclasts with heterogeneous extinction exhibit cracks and cavitary fractures (1, Fig. 8B). Quartz phenocryst margins appear impacted with recrystallized rims and fluid inclusions. Sub-rounded quartz shows anomalous birefringence of kink bands along sheared planar fractures and partial isotropization with sub-parallel lamellae (2, Fig. 8B). In sub-rounded clayey chondrules, sub-angular feldspar phenocrysts with cavitary fractures have been sheared and crushed along the margins in a devitrified brown matrix (Fig. 8C). Crushed clast margins in shearing context show clastic matrix mixture and recrystallized asymmetric tridymite in a devitrified matrix. We observed asymmetric deformations of quartz spheroids in cataclastic shear bands and cavities of quartz dehydration with mosaicism extinction in matrix mixture (Fig. 8C).

~~4.5.~~4.5 XRD and SEM analyses of the coating matrix

The XRD patterns of clayey brown matrix from three samples of coated clasts show sharp peaks of specific mineralogical assemblages (Fig. 9A). Clay minerals such as kaolinite, smectite and illite are associated with quartz and albite. Similar clayey assemblages occurred in each structural unit. Fig. 9B compares the XRD patterns of the inner (2) and outer rims (3) of dacite clasts (1) in DC (L = 12 km). We observe the occurrence of quartz with plagioclase and magnetite. The inner pseudotachylite rim (~6% of the volume) is related to a vitreous phase with magnetite. The outer rim with cataclastic bands (~1.2 to 6% of the volume, Farquharson et al., 2016) shows the occurrence of quartz, plagioclase and magnetite. There is an inverted crystallinity gradient related to concentric rim structures and reverse grading (Fig. 9B). The magnetite is absent in the inner rim, whereas sharp peaks of quartz and plagioclase are identified in the outer rim with cataclastic bands.

alt-text: Fig. 9

~~Fig. 9.~~Fig. 9

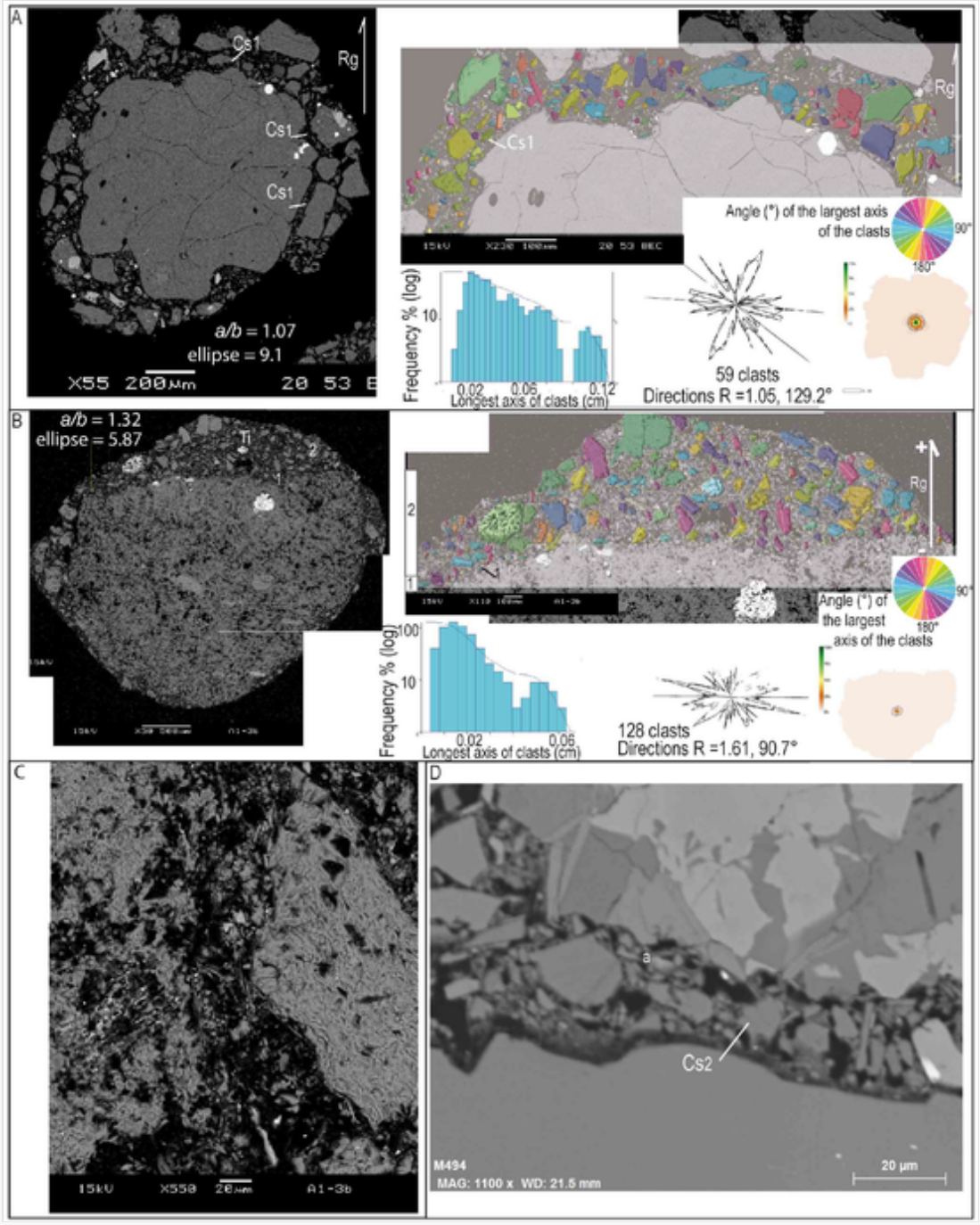


X-ray diffraction patterns (UCA-START-DRX in Clermont) of coating matrix. A. X-ray diffraction patterns of clayey brown matrix from three matrix samples between 7.4 and 12 km runout distances; B. X-ray diffraction patterns from thin section of the coated dacite clasts (1, ~8 mm in diameter) from DC showing the pseudotachylite inner rim (2) and the outer rim with bands and linear flow texture (3). (For interpretation of the references to colour in this figure legend, the reader is referred to the web version of this article.)

Microstructures of coated clasts are differentiated by detailed SEM observations (Fig. 10). Bands with linear flow texture (~31–47 wt% SiO_2 with 14–17% matrix, Table 3, Fig. 10A) and reverse grading along the subrounded coated clast shows a polymodal distribution and a preferred alignment of clast long-axes deduced from SPO analysis (ellipse/a/b = 8.5). Undulating sheared contacts with reverse grading present bimodal clast distributions and clast long-axis inclinations between 23- and 160° (ellipse/a/b = 4.44, Fig. 10B) oblique to the megaclast. Embayment boundaries along crushed clast margins are related to a shearing context with hydrothermal alteration between 12 and 24 wt% SiO_2 (Table 3, Fig. 10B–C). Microfractures are filled with 73–79% matrix and crushed clasts showing parallel alignment of acicular nepheline around ~9.5 wt% SiO_2 and ~2 wt% $Na_2O + K_2O$ with low values of Al_2O_3 (~3 wt%) and MgO (~1 wt%, Table 3, Fig. 10D).

alt-text: Fig. 10

~~Fig. 10.~~Fig. 10



Microstructures of coated dacite clasts shown in SEM images with SPO analysis. A. Polymodal bands (Cs_1) with linear flow texture around 14–17% matrix and 31–47 wt% SiO_2 (Table 2) show preferred alignment of phenocrysts with long-axis inclination of ~129° (SPO from 59 clasts with $a/b = 1.07$, ellipse = 9.1). Undulating and sheared contacts (*white dotted line*) with reverse grading (Rg) present bimodal clast distributions; B. Two bands with linear flow texture (1–2 in *yellow dotted lines*) and bimodal clast distributions (SPO from 128 clasts, $a/b = 1.32$; ellipse = 5.87) related to clast long-axis inclinations between 23- and 160°. We observe titanium oxide (Ti) with hydrothermal alteration and embayment boundaries along crushed clast margins (~12–24 wt% SiO_2, Table 2); C. Hydrothermal alteration of sheared clasts; D. Secondary bands (Cs_2) and microfracture with 73–79% matrix generating parallel alignment of acicular nepheline. (For interpretation of the references to colour in this figure legend, the reader is referred to the web version of this article.)

alt-text: Table 3

~~Table 3.~~ Table 3

The table layout displayed in this section is not how it will appear in the final version. The representation below is solely purposed for providing corrections to the table. To preview the actual presentation of the table, please view the Proof.

Electron microprobe analysis (wt%) of different lithofacies observed in coated clasts and clayey chondrules.

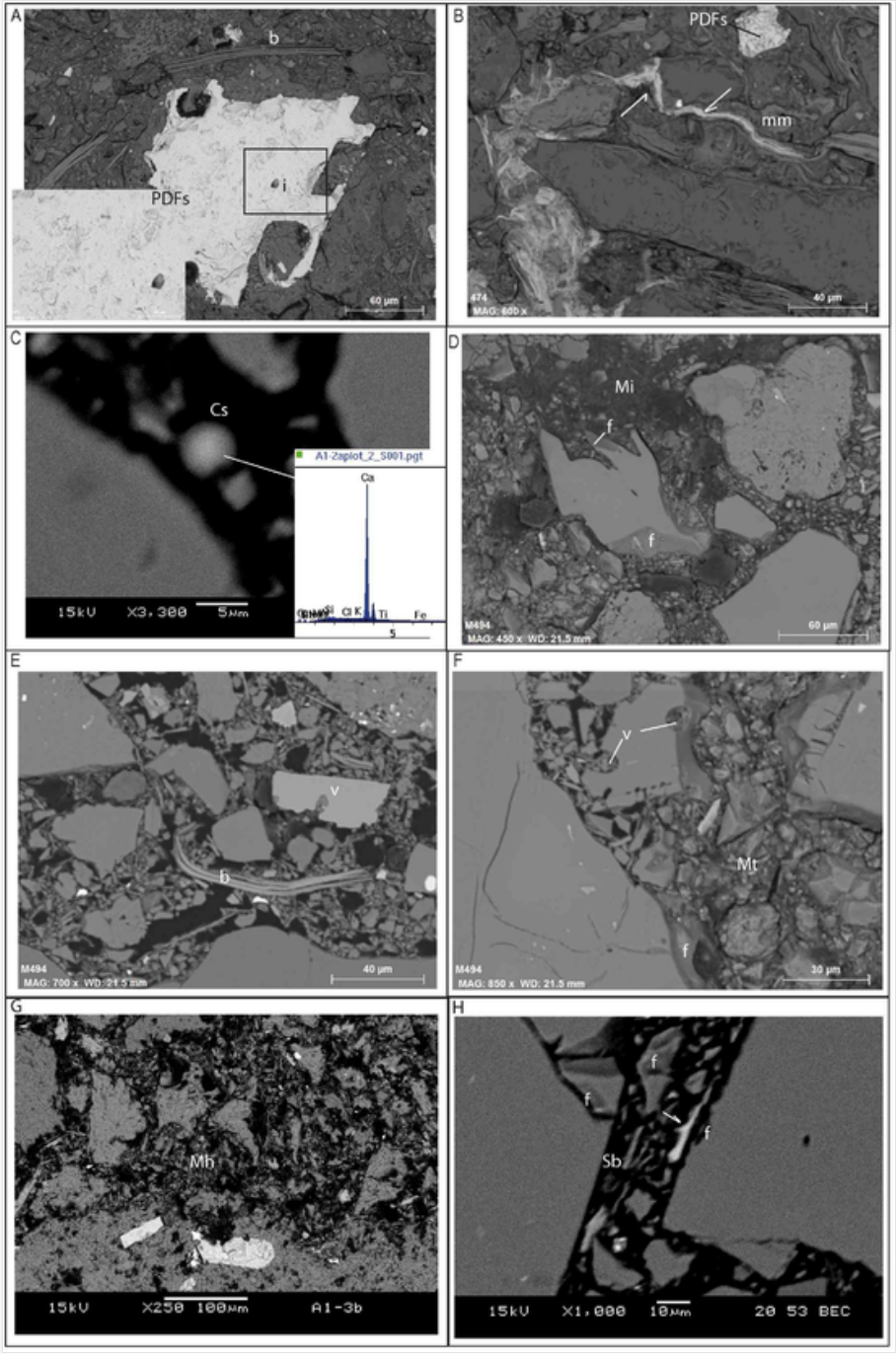
Major elements (wt%)	SiO_2	TiO_2	Al_2O_3	$FeO+Fe_2O_3$	MnO	MgO	CaO	Na_2O+K_2O	Total

Coated clast									
Clast	84.88	0.06	8.34	0.31		0	0.39	6.03	100
	28.06	0	9.09	0.21		0.02	2.62	2.1	100
Rim matrix	65.63	0	21.98	0.44		0	7.99	3.96	100
Rim phenocrysts	48.43	3.42	17.9	14		5.14	0.94	10.06	99.99
Cataclastic shear bands (13)	31.48–47.02	0.02–0.14	4.32–11.76	0.13–2.79		0–0.5	0.02–5.37	1.73–6.22	100
Hydrothermalized clasts (25)	12.08–24.24	0.57–3.78	3.81–4.95	5.1–11.42		0.69–4.19	0.46–8.58	0.43–2.03	100
Hydrothermalized spheroids (2)	21.89	0	8.42	0.15		0.02	3.47	1.32	100
Acicular phenocrysts(5)	9.54	0.64	3.22	2.46		0.95	0.03	2.35	100
Clayey clasts									
Cataclastic matrix 36–60%	49.31–51.76	0.32–0.37	17.96–28.74	3.04–4.54	0.18	2.33–6.1	2.15–3.29	5.98–6.05	96
72–80%	55.34–83	0.23–1.7	15.29–17.83	2.37–16.39	0.09–0.27	0.26–7.92	1.57–5.81	6.38–7.97	100
Thermic matrix 59–68%	52.86–65.36	1.39–1.6	14.4–16.79	13.41–23.29	0.1	4.47–5.97	1.88–2.33	4.85–6.65	107
68–81%	56.85–77.68	0.33–1.65	12.92–25.12	0.73–12.86	–	0.11–4.21	1.55–8.17	4.79–9.84	102

Detailed SEM observations isolate the characteristics of matrix coating (312 analyses, Fig. 11, Table 3). Planar Deformation Features (PDFs, Fig. 11A) are observed in titano-ferric oxide. Fig. 11B shows melting fissures of potassic feldspar with manganese oxide in clastic and different matrix showing finer-grained matrix with melting zones and PDF-bearing titano-ferric clast with large conchoidal striations. Calcic spheroids around ~5 μm in diameter (Fig. 11C) are observed in a clastic flux. Interclastic melt pockets (Fig. 11D) characterize the absence of linear flow texture between 36- and 60% matrix and 49–51 wt% SiO_2. We observe conchoidal and hydraclastic fractures along clast margins, melt-corroded clast related to thermal effect (Fig. 11D). Albite and nepheline occur in ~36% clastic matrix and they partly reacted to form jadeite ($NaAl(Si_2O_6)$, $KAl(SiO_4)$) as concomitant with hydrojade leaching ($AlSi_3O_7$) and chloritization. The ductile deformations of biotite and cavitary vesiculations of hydraclast (Fig. 11E) are observed between 59 and 68% matrix with 59–68 wt% SiO_2. The secondary hydroclastic fracturing is identified between 61 and 77% matrix with 56–77 wt% SiO_2 (Table 3, Fig. 11F): cavitary vesiculations of hydraclasts and secondary conchoidal fractures along clast margins contribute to matrix transformations. We describe secondary hydrothermal alteration of transformed matrix around ~49% (Fig. 11G). Planar microfractures occur in secondary and transformed matrix around ~73–79% with a preferred alignment of the clast long-axes showing hydraclastic fractures along clast margins and partial melting of acicular titanium oxide (Fig. 11H).

alt-text: Fig. 11

~~Fig. 11.~~Fig. 11



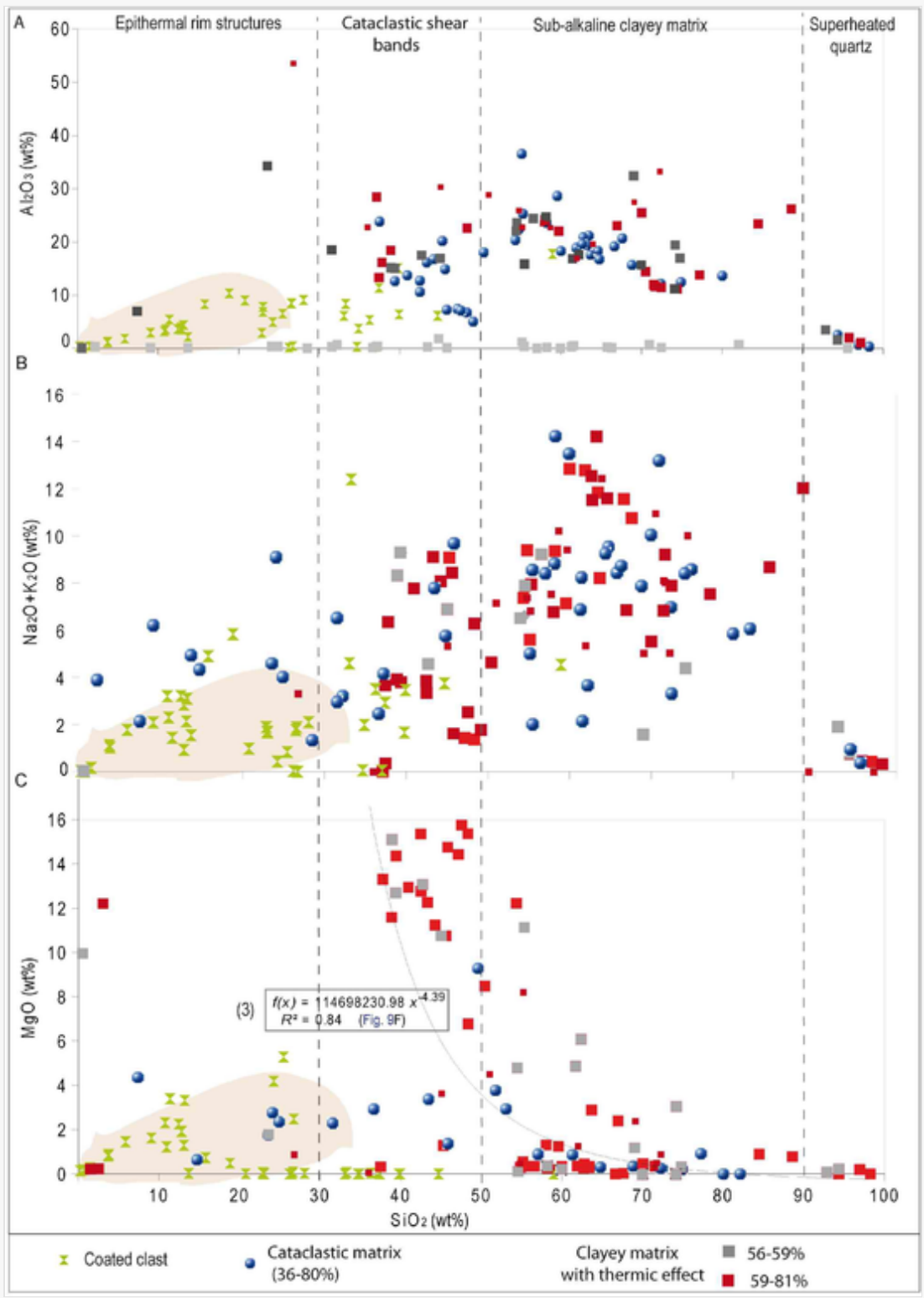
Matrix lithofacies shown in SEM images. A. Planar Deformation Features (PDFs) observed in titano-ferric oxide (~85 wt% FeO and 14 wt% TiO_2) with ferric fluidal inclusion (i, 94 wt% FeO and 15.5 wt% SiO_2) and ductile deformation of biotite (b); B. Melting fissure of potassic feldspar indicated by *white arrows* with manganese oxide (37 wt% MnO and 19 wt% SiO_2) in clastic and different matrix (mm) showing finer-grained matrix with melting zones and PDF-bearing titano-ferric clast (PDFs) with large conchoidal striations; C. Microprobe analysis of calcic spheroids (Cs, diameter ~5 µm; 30 wt% CaO and 68 wt% CO_2) in sheared clastic flux; D. Interclastic melt pocket (Mi) inside 50% matrix with conchoidal and hydraclastic fractures (f) along clast margins; E. Ductile deformation of biotite (b) and cavitary vesiculations (v) of hydraclast observed in 59–70% matrix between 52 and 65 wt% SiO_2; F. Transformed matrix (68 wt% Mt, 56–77 wt% SiO_2) showing cavitary vesiculations (v) of hydraclast, secondary conchoidal fracture (f) along clast margins; G. Secondary hydrothermal alteration of transformed matrix around ~49% (Mh); H. Bands (Sb) in secondary clastic matrix with preferred alignment of clast long-axes showing hydraclastic fractures (f) along clast margins and partial melting of acicular titanium oxide indicated by *white arrow*.

SEM investigations (312 analyses, Table 3) differentiate major element compositions in the matrix lithofacies. The mean composition of all samples is ~48.1 wt% SiO_2, ~13.5 wt% Al_2O_3, 4.9 wt% Na_2O+K_2O and ~2.4 wt% MgO. Rim structures of the coating matrix have the lowest SiO_2 and Al_2O_3 contents (3–21 wt%).

The sub-alkaline clayey matrix shows a wide range of their SiO_2 (49–77 wt%, Fig. 12) and Al_2O_3 (13–28 wt%) abundances. Few elements (191 analyses, Table 3) in the matrix samples are recurrent in 60% such as ~0.71 wt% IrO and ~0.35 wt% of Au_2O.

alt-text: Fig. 12

~~Fig. 12.~~Fig. 12



Chemical variation diagrams of Al_2O_3, Na_2O + K_2O and MgO *vs*. SiO_2 (wt%) contents of coated clasts compared to different lithofacies in clayey chondrules.

Chemical variation diagrams of Al_2O_3, Na_2O + K_2O and MgO *vs*. SiO_2 contents (Fig. 12) of coated clasts are compared to different matrix lithofacies in clayey chondrules. The matrix samples can be subdivided into four distinct SiO_2 subgroups related to microstructures: epithermal rim structures including crushed margins and incipient melting (3–21 wt% SiO_2 and Al_2O_3); bands with linear flow texture (~31–47 wt% SiO_2); sub-alkaline clayey matrix with interclastic melt pockets and clastic vesiculations (~49–77 wt% SiO_2, 13–28 wt% Al_2O_3); superheated quartz spheroids (>90 wt% SiO_2). We differentiate the secondary bands (Cs_2, Fig. 11G) with microfractures related to 73–79% clayey matrix and 11.2–34.2 wt% Al_2O_3 (Fig. 12A).

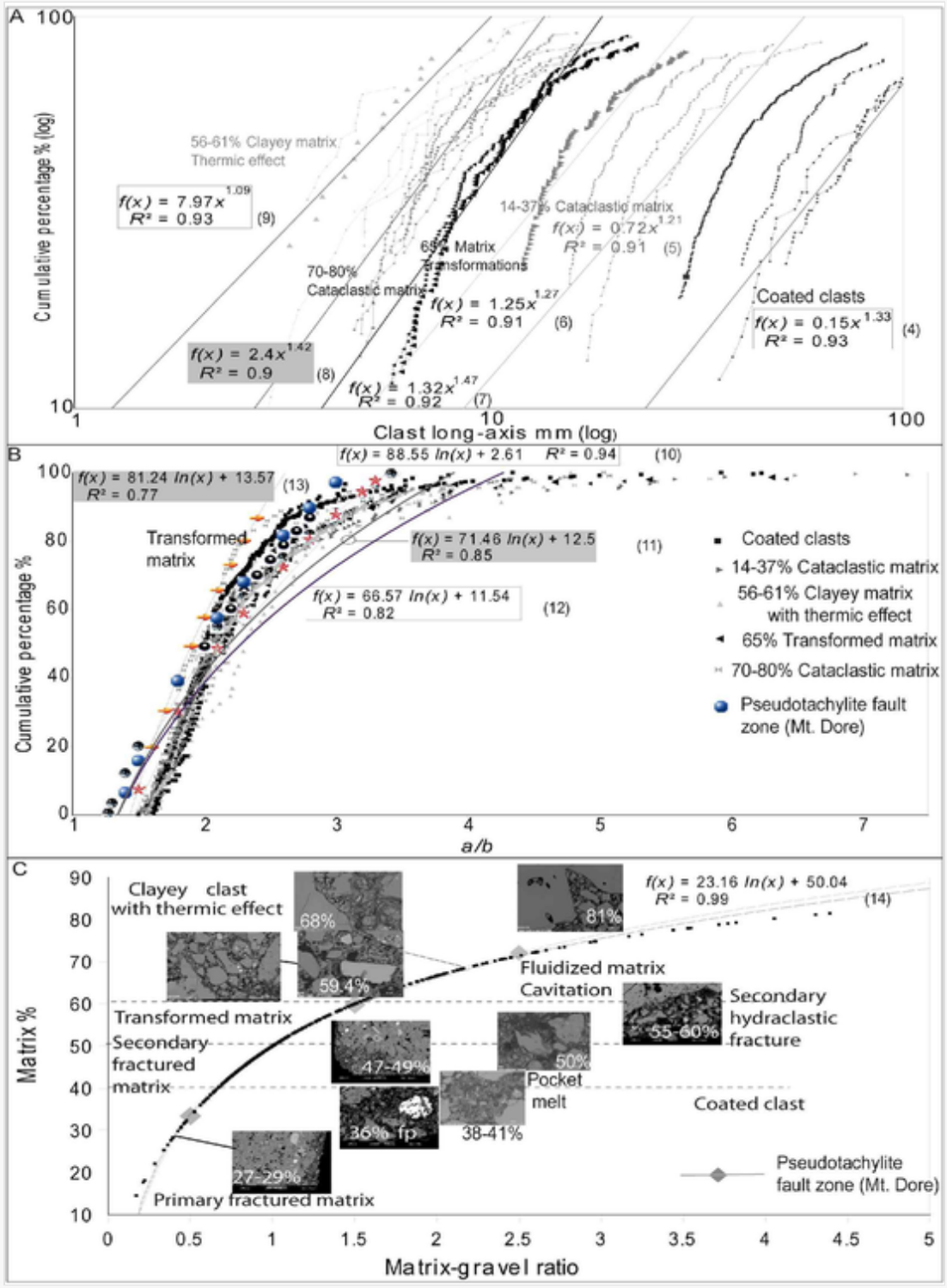
Interclastic melt pockets observed in 36% clayey matrix (Fig. 11D) exhibit 40–50 wt% SiO_2 with decreasing Al_2O_3 from 20 to 5 wt% (Fig. 12A) and increasing values of Na_2O + K_2O from 2 to 10 wt% and MgO from 1 to 6 wt% (Fig. 12B-C). A power regression of MgO (Eq. (3) in Fig. 12C) characterizes the ductile deformations and the cavitary vesiculations around ~56% matrix between 59- and 68 wt% SiO_2 (Figs. 11E–F and 12). The values of Al_2O_3 and Na_2O + K_2O are similar. The low values of MgO (<1 wt%) are close to those obtained in the transformed matrix between 56- and 77 wt% SiO_2 showing secondary fracturing along clast margins (61–77% matrix, Fig. 11F).

~~4.6.~~4.6 Sedimentology of the inner and outer rim of clasts

To compare clast-size fractal distributions related to matrix percent, fractal *h* and *D* values are estimated from the power regressions of cumulative frequency on double-logarithmic graphs (Eqs. (4)–(9) in Fig. 13A). A progressive evolution of cataclastic matrix between 14 and 70% is correlated to matrix microtextures compared to coated clasts. Calculated fractal *D* values are between 0.45- and 0.54 for the 14–37% cataclastic and fluidized matrix in the 12.2 to 63.58 µm clast-size range, 0.82 for 56–61% clayey matrix with thermal effect in the 5.8–16.8 µm clast-size range, 0.052 for the 65% transformed matrix in the 5.81–21.5 µm clast-size range, and 0.146 for the 70–80% cataclastic matrix in the 4.7–16.2 µm clast-size range (Fig. 13A). The coated clasts are characterized by a power regression (Eq. (4) in Fig. 13A) with negative fractal *D* values between –0.24–0.51 in a range from 34- to 142 µm. The cumulative curves of matrix lithofacies *vs*. *a*/*b* (Fig. 13B) help to distinguish the coated clasts compared to the different lithofacies between 14 and 80% of matrix. These are characterized by four logarithmic regressions (Eqs. (10)–(13) in Fig. 13B), close to the regressions for the pseudotachylite lithofacies (50–80% matrix with $a/b = 2–3$, Bernard and van Wyk de Vries, 2017) in French Massif Central.

alt-text: Fig. 13

~~Fig. 13.~~Fig. 13



Sedimentology of the coated clasts shown in SEM images. A. Cumulative % *vs*. long clast-axis on double log graph; B. Cumulative curves of matrix lithofacies *vs*. *a*/*b*; C. Matrix % *vs*. matrix/gravels related to microtextural observations of coated clasts in SEM images.

The matrix percent *vs*. matrix/gravel diagram shows a logarithmic regression (Eq. (14) in Fig. 13C) related to microtextural variations of coating matrix from brecciation up to matrix transformations. We characterize (1) the primary fracturing with <40% coating matrix showing bands around 14–17% of the cataclastic matrix mixture, before pseudotachylite impact around 28% matrix. Partial melt is observed with ~36% of crushed matrix showing sub-rounded fractured magnetite and embayment boundaries related to thermal effect. (2) The secondary fracturing between 40 and 50% breccia matrix is identified along crushed clast margins with embayment boundaries and pockets of melt around 38–50% matrix. (3) Matrix transformations are characterized by 55–60% hydroclastic breccia matrix. These are similar to the impact-sheared contact of avalanche fault zone (Bernard and van Wyk de Vries, 2017). (4) Fluidization between 60 and 70% matrix in clayey chondrules is associated with cavitation and thermal effect between 59- and 68% matrix. Embayment boundaries show secondary fracturing around 61–68% matrix with clastic flux at 73–79% matrix and fluidization by cavitation around 81% matrix.

~~5.~~5 Discussion

Lithofacies and sedimentary analysis of the coating matrix help to identify fragmentations and transport processes in the 2010 Mount Meager avalanche transformed into a highly mobile debris flow. Statistical grain-size parameters and SEM investigations contribute to characterize concentric rim structures of coated clasts and clayey chondrules related to temperature pressure regime. Sequential events of microfabric formation along avalanche fault zone have been established and correlated to the proximal flow regime during impact wave.

~~5.1.~~5.1 Avalanche brecciation and faulting

The proximal avalanche disaggregation into highly mobile debris flow (M ~2.5, v = 54–109 m/s, Guthrie et al., 2012) appears different to the flood surges of the Cascade magmatic arc (v ~30 m/s, Mount Rainier, Mount Saint Helens in the USA, Scott et al., 1995), or avalanche dam break-outs (v ~15 m/s, Nevado de Colima volcano in Mexico, Capra and Macías, 2002), or the progressive avalanche transformations into lahars (v ~25–22 m/s with >3–5% clay, Iliamna Volcano, Alaska, Waythomas et al., 2000). A switch from frictional to the Voellmy rheology, modeled as a turbulent and sliding friction with the entrainment of saturated material, may change the granular mass and pore fluid pressure with water fluidization related to transition from avalanche to debris flow (McKinnon, 2008; Guthrie et al., 2012).

An inverted cataclastic gradient related to clast sizes in the matrix breccias (as deduced from SPO analysis, Bernard et al., 2019) is correlated between these structural units: from the mixed matrix lithofacies in MB, then the reworked flow breccias in the upstream diluted tail (TS, A in Fig. 2), the thrust and crushed surface with jigsaw fractures of lava blocks and fold of matrix breccias in PL (C-D in Fig. 2), to southeast blocks rafted in hybrid avalanche deposits transformed into debris-flow

deposits in DC. The sandy-gravelly texture becomes gravelly. Thrust and folds of matrix breccias are associated with basal bulking at the front of the thrust unit (C in Fig. 3). The mixed lithofacies (E in Fig. 3) is reworked into debris-flow deposits.

Matrix breccias with reverse grading imply a specific fragmentation of coated clasts along the sheared contact between the rock-avalanche deposits and debris flow. Avalanche brecciation and faulting during mass spreading may contribute to the fluidized decoupling and the distal fluidized outburst with progressive dilution into hyperconcentrated flows (Guthrie et al., 2012). Jigsaw breccias and blocks are observed in the mixed matrix at the upper, frontal lobe (Figs. 1–2). The secondary hybrid avalanche deposits in DC show rafted blocks in the mixed matrix. These are related to the frontal sorting of 30–40% of coarser critical particle segregations in the flow head (Kokelaar et al., 2014). Aggradation along the distal front of the thrust lobe and secondary fracturing along fault zones contribute to transformation and *syn*-transport fluidization of hydroclastic breccia matrix (>65%) generating debris flow surge and hybrid avalanche deposits in downstream.

Self-organization in granular flow with structural control may be envisaged from extensional to thrust zones observed in structural unit TS. Cataclastic injections and matrix accommodation along bands imply a rapid deposition with structural readjustments. The mixed and fluidized matrix may affect the non-uniform distribution of pore fluid pressure with low values of friction coefficient (~0.06, Davies and McSaveney, 1999; Collins and Melosh, 2003; Guthrie et al., 2012). Oscillatory stress with frictional variations changed the vertical velocity. These transformed lithofacies show *syn*-transport granular evolution with distal fluidization.

~~5.2.~~5.2 Lithofacies evolution of rock avalanche-debris flow deposits

~~5.2.1.~~5.2.1 *Cataclastic gradient*

The comparison of each grain size-fractions with cumulative curves, and histograms (Fig. 4) helps to identify the matrix lithofacies and the avalanche transformations related to an inverted cataclastic gradient. The grain-size fractions decrease between the poorly sorted lithofacies in MB and the transformed deposits at the front related to the reworking of avalanche deposits along the fault zones. The coating matrix contributes to uni- and bimodal clast-size distributions of debris-flow lithofacies at 89% (Fig. 4) and the increase in a/b ratios from 1.25 to 1.54. The pebble fractions (~3–4 Φ) of debris-flow lithofacies increase from 19 to 63%, while the coarse sand fractions are absent. The distribution of the coated clasts may contribute to the proximal fluidized disaggregation (McKinnon, 2008) of rock-avalanche with high clay contents related to hydrothermal alteration.

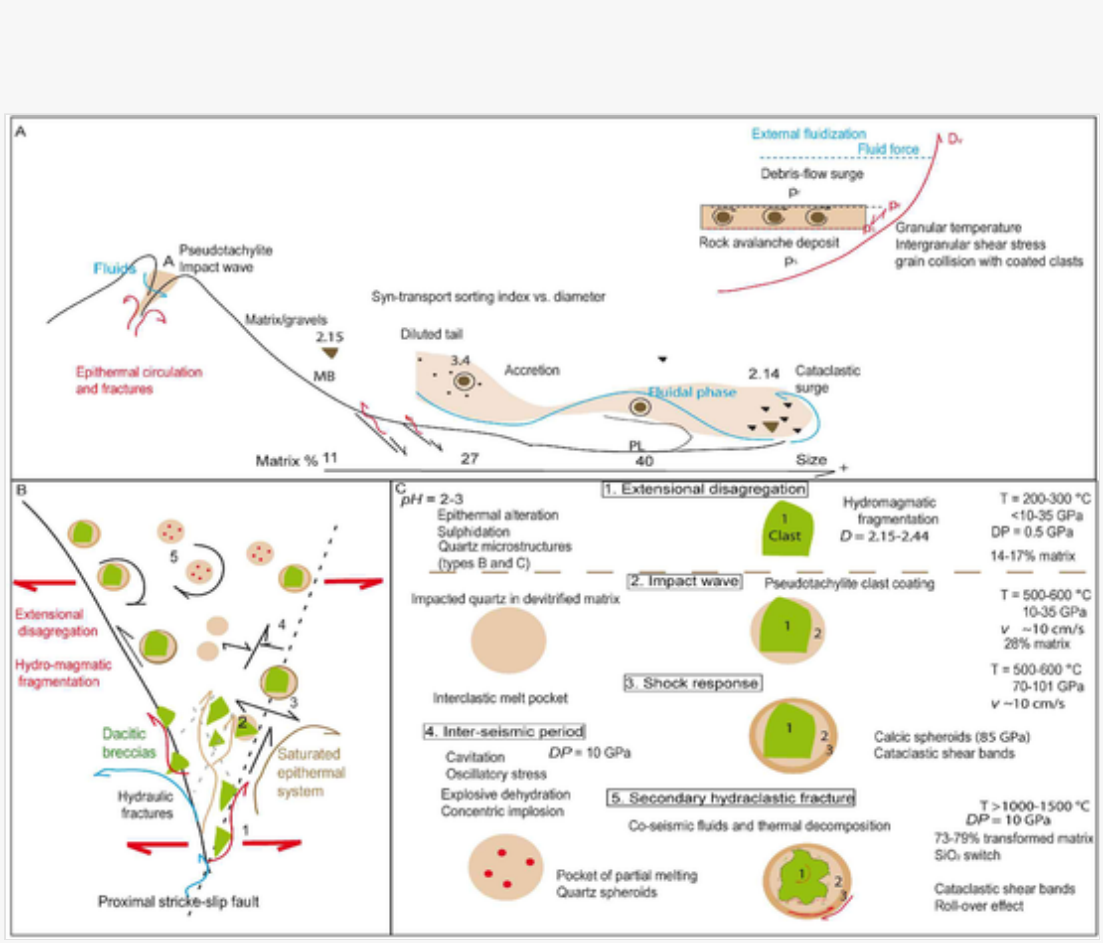
Ellipse/a/b values between 1.5 and 2.5 with the increase matrix content from 27 to 40% characterize the reworked avalanche deposits and evidence of the transformation into debris-flow (Bernard et al., 2019). The polymodal grain-size distributions of the secondary hybrid avalanche deposits in DC may interact with basement during the frictional flow propagation (Hungr and Evans, 1996). A logarithmic regression (Eq. (2) in Fig. 7) characterizes the perimeter roughness *vs*. clast size diagram for the clasts of the rock avalanche-debris flow deposits. Cataclastic sorting contributes to increase the variations of the perimeter roughness from 1 to 2.9 between MB to DC. The largest coated clasts (>32–16 mm) have been remobilized along the thrust contacts increasing the perimeter roughness. These values are similar to those of lava breccias of the Tutupaca fault ridges and Alto-Jesus sheared sigmoids in Peru, related to comminution and cataclastic gradients of crushed breccias in a fluidized matrix (Bernard et al., 2017, Bernard et al., 2019). *Syn*-transport evolution of coated clasts must be considered.

~~5.2.2.~~5.2.2 *Syn-transport sorting*

The sorting index (σ) *vs*. median diameter (Figs. 5B and 14A) diagram helps to identify the avalanche dam-breakout deposits (68% of samples with σ <1.5 and *Md* <–2 Φ, Capra, 2007), and the hybrid avalanche matrix between –2 and –1 Φ. The transformed deposits into the debris-flow lithofacies (*Md* >–2 Φ, Fig. 5 B) have similar values to the Pinatubo lahar deposits for 34% of samples (σ ~2.2, Table 2, Major et al., 1995) and parallel to the channelized and diluted lithofacies of the San Lazaro thrust lobes in Peru (*Md* >–1 Φ, Bernard et al., 2017). We differentiate the medium sandy fractions (>0 Φ; γ = 0.48–0.69) suggesting a transport by traction in TS, and the coarser sandy fractions (<–1 Φ; γ ≥–0.48) with a transport by saltation and suspension (Table 2, Wohletz et al., 1989; Bernard, 2015).

alt-text: Fig. 14

~~Fig. 14.~~Fig. 14



Sequential events along rock avalanche-debris flow deposits. A. Cataclastic evolution of lithofacies; B. Injection vein related to sequential coating stages in C; C. Sequence of events related to matrix percent and temperature pressure regime.

Sub-rounded coated clasts contribute to reduce the flow strain related to cataclastic *syn*-transport sorting (σ ~ 0.99–1.45, Figs. 5B and 14A), associated with structural control, collisional regime and comminution (Caballero and Capra, 2011) during fluidized disaggregation and leaching of the finer grain-size fractions (lahars of Pemberton in Canada, Simpson et al., 2006). The granular mass and pore fluid pressure may change during the switch from frictional to the Voellmy rheology with a differentiated expansion of the initial volume (7–26%, Nomash slide, Vancouver Island in Canada, Hungr and Evans, 2004) and water fluidization related to transition from avalanche to a saturated flow.

These appear very different to the flood surges of the Cascade magmatic arc with porosity between 14 and 28% and saturation from 45 to 92% (Mount Saint Helens volcano, Washington in the USA, M ~ 5.1, G1icken, 1986; Mount Rainier, Cascades Arc in the USA, Vallance and Scott, 1997). The transition from cohesive to non-cohesive lahars with rounded coarse fractions is not observed (*SKg* from 0.85 to 1.5; σ = 3.4–5.25, Table 2, Scott et al., 1995; Vallance and Scott, 1997). Sorting index and skewness values are not related to avalanche dewatering and granular disaggregation (Major and Voight, 1986; Capra, 2007). With the runout distance, the skewness and kurtosis values decrease except in PL, while the fractal *D* values increase from 2.15 to 2.44 (Table 2). The transformations in the matrix mixture have resulted in higher skewness and kurtosis values as observed in the Ruapehu, Chimborazo and Ticsani DADs (*SKg* = 0–0.55; *K* = 1–1.07, Table 2, Bernard, 2008; Keigler et al., 2011; Bernard, 2015; Bernard et al., 2019). Dilution and sorting have induced lower skewness values (<–0.1, Table 3) for the flow breccias in the diluted tail (TS) and the downstream thrust lobe (DC).

~~5.2.3.~~5.2.3 *A similar cataclastic origin*

A similar grain-size distribution of the sandy-gravel matrix and the power regression between matrix percent and matrix/gravels (Eq. (1) with $R^2 = 0.98$ in Figs. 5A and 14A) implicate a similar cataclastic origin with a co-genetic evolution of lithofacies. These values of the sandy-gravel matrix are close to those of the sandy layer before the impact-sheared contact along avalanche fault zone in French Massif Central (Bernard and van Wyk de Vries, 2017). The increasing *D*-values related to the percentage of matrix (MB, DC) and matrix-gravel ratio are related to jigsaw fit-textures (<10.3% matrix), and the primary fracturing (~41% matrix, MB-TS) with 40 to 50% *syn*-emplacement breccias along the downstream thrust lobe (TS and DC, Fig. 14A). The matrix percent *vs*. matrix/gravels diagram helps to distinguish primary fracturing from thermal effect such as melt-corroded clast around ~61% (bx2 units, Hickson et al., 1999), dilation and shear fracturing with 22% matrix, close to the Tutupaca lava breccias in Peru (Bernard, 2015). The secondary fracturing between 73 and 79% matrix is related to the hydromagmatic fragmentation of the polymodal hybrid deposits (γ = 0.4 + 0.4 in DC, σ ~ 2.43, Wohletz et al., 1989), showing coating matrix with secondary bands and microfractures (Fig. 10). The parent volcanic processes include the pyroclastic domain (γ = 0.5–0.97, Vulsinni, Taddeucci and Palladino, 2002; γ = 0.8–0.2, Mount Saint Helens, Mackaman-Lofland et al., 2014) for 57% of the granular fractions around –1.6 Φ (Figs. 5–6, Supplemental file 1). The avalanche deposits in Peru and Canada present similar γ-values between –0.1 + 0.2 (Bernard, 2015). We differentiate the avalanche deposits in subduction zones. These deposits appear between the reworked Pardines deposits in French Massif Central (*Kg* = 1, *SKg* = 0.1-0.2) and Tutupaca avalanche deposits in Peru (*Md* = 3-2 Φ, σ = 1.25), in accordance with energy fragmentation/energy potential *vs*. *D* values (Bernard et al., 2019).

~~5.3.~~5.3 Epithermal clast coating

~~5.3.1.~~5.3.1 *Concentric rim structures*

Microstuctural investigations (312 analyses, Table 3, Figs. 10–11) differentiate the inner rim of coated clasts (8 cm to 1 mm) from their border and the surrounding matrix. Concentric rim structures may be associated with hydromagmatic fragmentation generating vitroclastic matrix, hydraclastic microfractures with interclastic melt pockets, partial melting, cavitary vesiculation of hydraclasts and ductile deformation of biotite. We differentiate the inner rim (<35%, a/b < 1.8–3) around 28 wt% SiO_2 and polymodal bands with linear flow texture (Fig. 10A, Farquharson et al., 2016) and reverse grading (a/b = 3–7, 31–47 wt% SiO_2, Fig. 13C). This cataclastic mixture of matrix between 14 and 17% is related to primary fracturing (<40% matrix) including a colloidal Al_2O_3 gel between 11 and 28%, which contributes to the accretionary coating. These may be related to lamellar plasma spraying (0.7 MPa, 55 V, Goral et al., 2013) with partially melted regions. The concentric rim structures may be generated by Al_2O_3 precipitation between two $Si(OH)_4$ laminae (~10 Å) with circulation of K^+ and H_2O (~7 Å).

Extensional disaggregation related to hydromagmatic fragmentation of dacite clasts can be distinguished (γ = 0.1 + 0.2, Wohletz et al., 1989; *D* = 2.15–2.44, Tutupaca and Misti in Peru, Bernard, 2015) with ellipse/a/b values between 1.02 and 4.05. We differentiate the thermal effect of fragmentation with ellipse/a/b < 1.7 (Bernard et al., 2019). Embayment boundaries increase the inner roughness of sheared clasts, while the values of the outer sphericity of the coated clasts increase (DC, Fig. 6). These are related to secondary inner fracturing between 47 and 49% breccia matrix with shear flow variations along reworked contacts generating a roll-over effect. Transformed matrix is between 61- and 77% with 56–77 wt% SiO_2. Microfractures and secondary bands with 73–79% fluidized matrix generate parallel alignment of acicular nepheline in basaltic melt around 9.5 wt% SiO_2 (Table 3, Fig. 10D). *Co*-seismic fluids contribute to secondary hydraclastic fracturing generating transformed matrix between 55- and 60% (Fig. 11D–F) with interclastic melt pockets.

~~5.3.2.~~5.3.2 *Epithermal alteration*

Clayey mineral assemblages identified by XRD patterns (Fig. 9A) are related to the brown matrix lithofacies, similar to the water-saturated and hydrothermally altered volcanic rocks observed along the west lateral scarp (Guthrie et al., 2012). The partial hydrolysis of plutonic and metamorphic basement may produce kaolinite 1/1 from feldspar, smectite 2/1 from biotite and illite. The clayey matrix implies epithermal breccia zones with acid-hydrothermal circulation (Friele and Clague, 2004; John et al., 2008; Guthrie et al., 2012) and alteration along fractures. Smectite clays may swell by water adsorption, generating extensional dilation and decreasing permeability of a rock mass (Friele and Clague, 2004; Heap et al., 2017, 2020). Chlorite can occur as a result of epithermal alteration and lubrication of the fracture planes, a precursor stage to the proximal collapse in fault rocks along the unstable slopes in MMVC (Friele et al., 2005).

These are in accordance with saturated avalanche and debris flows observed in the MMVC eruptive rocks (mafic to felsic volcanic rocks, M7, Hickson et al., 1999; Friele and Clague, 2004; Simpson et al., 2006; PY3, Russell et al., 2007; Friele et al., 2008; Mount Rainier, John et al., 2008), linked to subduction-zone volcanism. Metal sulphide traces such as Au_2O and IrO are associated with epithermal systems (200–300 °C) from continental and magmatic systems in exhumed formations, near convergent plate boundaries (Ingebritsen et al., 2010). The initial particle size distributions, electrostatic and hydrostatic bonding forces, hydrothermal conditions, Reynolds numbers of the fluidized particles and external water contribute to the coating layer thickness (PC1–2, Tenerife, Canary Islands; Tunguruhua volcano, Ecuador; Stromboli, Sabatini and Solfatare explosions, Italy, Mueller et al., 2018) of hydroclastic breccias in impact melt flow.

~~5.3.3.~~5.3.3 *Different conditions of temperature and pressure*

Temperature pressure regime (≥650 °C, >0 > 20 kbars, v > 10 cm/s, Weidinger et al., 2014) may be envisaged during primary shear propagation. The occurrence of a pseudotachylite vitreous phase with magnetite (Fig. 9B) and bands may implicate electric currents, related to differentiated conductivity (Ferré et al., 2005) between the clast margins and coating matrix. These include co-seismic fluids in rotational shear (Ferré et al., 2005; Magloughlin, 2005) related to dehydration of transformed cataclastic matrix around ~14 wt% FeO + Fe_2O_3 with epithermal effect (Table 3).

Calcic-rich spheroids (Fig. 11C) in a sheared and transformed matrix are associated with a shock response in epithermal vein such as CO_2 dissociation and release (68.55%, 85 GPa) generating shocked carbonate. A rapid and fluid decompression with thermal effect may contribute to crystallization of microlithes such as acicular titano-oxide with basaltic melt and glass (Mount Saint Helens volcano, Blundy and Cashman, 2005; *P* ~ 70–101 GPa, *T* > 1500 °C, Bezeava et al., 2016) at around 36% matrix. Secondary clastic flux may generate embayment boundaries along sheared clast margins including an epithermal effect such as a jadeite reaction (Figs. 6B, 10B–C, 11 and 13C).

Concentric implosion (~12–24 wt% SiO_2; <10 wt% Al_2O_3, Spray, 1999a, 1999b) and fragmentation zoning with flash heating during cavitation may contribute to secondary clastic flux with incipient melting. Fluidization around 73–79% matrix characterizes the secondary bands with microfractures. A silica switch may be considered between the pseudotachylite inner rim (~3–21 wt% SiO_2 and Al_2O_3 in Fig. 12) of the dacite clast and their borders with cataclastic bands (~31–47 wt% SiO_2). These include superheated quartz spheroids with hot emplacement of the vitroclastic matrix (bx2 units, Hickson et al., 1999).

~~5.4.~~5.4 Clayey chondrules

The sub-alkaline clayey matrix shows a wide range of their SiO_2 (49–77 wt%, Table 3, Fig. 12A–C) and Al_2O_3 (13–28 wt%) abundances with metal sulphide traces (200–300 °C, Au_2O, IrO). Few primary cataclastic stages between 14 and 17% cataclastic matrix mixtures imply co-genetic relationships (Eqs. (10)–(13) in Fig. 13B) with coated clasts. A similar cataclastic evolution may be envisaged. We observe a linear flow texture of hydroclastic quartz, albite and biotite flake in devitrified brown matrix. The primary fracturing with a thermal effect (<56% matrix) is differentiated from the secondary fracturing with matrix transformations and fluidization (>65% matrix, Fig. 13C).

Quartz microstructures related to *syn*-seismic and post-seismic creep (Fig. 8, Trepmann and Stöckhert, 2003) are observed in a devitrified brown matrix: type B microstructures with microcracks, cavitary fractures and fluid inclusions; type C microstructures with kink bands and quartz recrystallization along microshear zones (<10–20 GPa). These have recorded a low temperature plasticity regime of 300–350 °C with peak differential stress of ΔP = 0.5 GPa and increasing water content related to fluid inclusions (Trepmann and Stöckhert, 2003). Seismic faulting generating brecciation along epithermal veins may be related to the precursor shear zone (Bestmann et al., 2011; Bernard and van Wyk de Vries, 2017).

We observe in a devitrified matrix anomalous birefringence of kink bands along sheared planar fractures and partial isotropization of shock sub-rounded quartz (10–35 GPa, Fig. 8B), microcracks and PDFs in titano-ferric oxide (~20–30 GPa, Fig. 11A–B, Bezeava et al., 2016; Reznick et al., 2016), and acicular nepheline (Fig. 10D). These can be related to near-stagnant conditions of the hydromagmatic system (Mount Taranaki, New Zealand, Turner et al., 2008). The glass transition temperature can be estimated around 500 °C in accordance with the calculated temperature for melted mica breccias (T ~ 650 °C, *pH* = 2–3, Spray, 1992), implying explosive decompression of exsolving volatiles with the hot emplacement of vitroclastic matrix (bx2 units, Hickson et al., 1999). An increase in the coating layer thickness is correlated to the effects of aluminium gel with *pH* ~ 2–3 and high viscosity binders (Mueller et al., 2018). Incipient melting and melting fissure of potassic feldspar in clastic and transformed matrix may be related to thermal decomposition (~1300 °C) and a silica switch between the inner rims (3–21 wt% SiO_2) and their borders (~31–47% SiO_2 in Fig. 12).

Pockets of partial melting may be related to decreasing values of Al_2O_3 (Fig. 12A) and coating effect. The values of Na_2O + K_2O increase from 2 to 10% and MgO from 1 to 6%. These are related to initial dilation and primary fracturing along dykes (36% matrix, 40–50 wt% SiO_2, Figs. 11D–F and 13C, Spray, 1992) during the late stage of the shock wave. Cavitation and clastic dehydration change the frictional temperature related to expelled co-seismic fluids (56–63% matrix; ΔP ~ 10GPa, *T* > 1000–1500 °C, Fig. 8, Spray, 1997, 1999a, 1999b; Bestmann et al., 2011; Weidinger et al., 2014), which decrease the melting point of the superheated quartz spheroids, as found for pseudotachylite fault zone (Bernard and van Wyk de Vries, 2017). These conditions may contribute to plasticity deformation of biotite flake (Fig. 10E, Spray, 1992), incipient melt, migration and interclastic melt pockets. These may be associated with a power regression of MgO (Eq. (3) in Fig. 12C) around 56% matrix between 59 and 68 wt% SiO_2, including hydrojade leaching and chloritization (Fig. 11).

~~5.5.~~5.5 Sequential coating stages

Matrix breccias and debris flow surges are associated with the propagation of shock wave with an oscillatory relative speed of *v* ~ 50 m/s (McSaveney, 1978; Guthrie et al., 2012; Kaproth and Marone, 2014; Bernard and van Wyk de Vries, 2017) during the inter-seismic period and responses in epithermal vein (Fig. 14B) such as mechanical fluidization. Coating matrix in crushed breccias are characterized by fractal *D*-values (~1.24–2.43), temperature pressure regime in the conduit margin and sequential evolution related to shock epithermal faulting (Anthony and Marone, 2005; Lavallee et al., 2012).

Faults related to pseudotachylite result of brittle-viscous deformations including comminution, frictional heating and the interplay of visco-elastic forces around the glass transition (>400 °C.s^{-1}, Lavallee et al., 2015). The rim structures of the coated dacite clasts occurred in the inner fault vein (Bestmann et al., 2011) are differentiated from the surrounding matrix with the border vein. These are related to an extensional disaggregation (*D* ~ 0.052–0.82), and near dike epithermal conditions, similarly to the Osceola collapse crater wall of Mt. Rainier (John et al., 2008).

Specific conditions are differentiated from the impact wave to the inter-seismic period (Fig. 14B–C). (1) An extensional disaggregation (*D* ~ 2.15–2.44) of an epithermal border vein generates quartz microstructures and clayey assemblage (*pH* = 2–3, *T* ~ 200–350 °C, <10–20 GPa, ΔP ~ 0.5 GPa) with colloidal aluminium gel. (2) *We* differentiate impacted quartz produced during shock compression (~10–35 GPa), from the inner pseudotachylite rim (*v* > 10 cm/s) related to co-seismic frictional melting in the conduit margin. We include glass transition and microcracks in titano-ferro oxide (~20–30 GPa, *T* ~ 500–650 °C). (3) Shock response in epithermal vein (~85 GPa) is related to the outer rim with bands and linear flow texture. We observe calcic spheroids, CO_2 dissociation (~70–101 GPa, *T* > 1500 °C) and interclastic melt pocket with a jadeite reaction. (4) In oscillatory stress conditions, clastic dehydration and cavitation contribute to concentric implosion (Spray, 1999a, 1999b) and spherical decompression generating fragmentation zoning in a strong shearing context. (5) In clayey chondrules, the frictional

temperature changes with cavitation and co-seismic fluids, which decrease the melting point of the superheated quartz spheroids (ΔP ~ 10 GPa, T > 1000–1500 °C), including incipient melt and pockets of partial melting. *Co*-seismic fluids contribute to secondary hydraclastic fracture generating transformed matrix with interclastic melt pockets, bands with a roll-over effect for the inner rim of coated clasts.

A sequential evolution includes co-seismic fluids during hypervelocity impacts, the shock response of epithermal systems related to *in situ* modifications with oscillatory stress and sub-glacial interactions. An epithermal fault evolution in the breccia zones may be associated with a thermo-mechanical evolution of deeper structures generating the recurrent destabilizations in the MMVC with avalanche transformations into flood surges (Guthrie et al., 2012; Roberti et al., 2017).

~~6.~~6 Conclusions

Semi-quantitative sedimentological analysis contributes to characterize at different scales textural variations of the matrix sampled along the sheared contact between the rock avalanche deposits and trailing debris flow deposits. An inverted cataclastic gradient of crushed breccias in a fluidized and mixed matrix implies a structurally controlled flow regime with clast sorting and rapid deposition. The coating matrix changed the initial polymodal distribution of the debris-flow lithofacies. Clast shapes are related to cataclastic sorting during transport and fluidized disaggregation. A few equations have been established implicating the same cataclastic origin.

Hydromagmatic fragmentations of matrix coating are in accordance with continental subduction-zone volcanism such as epithermal breccias related to a fault evolution in the MMVC eruptive rocks. Quartz microstructures in clastic matrix mixture imply co-seismic faulting. A microstructural gradient and clayey epithermal assemblage are established related to colloidal aluminium gel and bands with linear flow texture. Epithermal shock responses with co-seismic fluids contribute to frictional melting in the conduit margin such as basaltic melt and glass with calcic spheroids and CO_2 dissociation. Secondary fracturing and flash heating during cavitation produce quartz spheroids in clastic matrix mixture and partial melting.

The sequential coating stages of the matrix breccias were correlated with fractal D-values, temperature pressure regime in the conduit margin. Specific conditions from the impact wave to the inter-seismic period contribute to constrain the proximal avalanche transformation into a debris flow surge. This will in turn help to explain the recurrent water-saturated rock avalanche deposits in MMVC generating recurrent lahar deposits near the town of Pemberton, at a distance of 65 km from Mount Meager.

Supplementary data to this article can be found online at https://doi.org/10.1016/j.jvolgeores.2020.106994.

Uncited reference

~~Bernard and Thouret, 2017~~

Declaration of competing interest

The authors declare that they have no known competing financial interests or personal relationships that could have appeared to influence the work reported in this paper.

Acknowledgments

The fieldwork in Canada trip has been funded by the French ambassador (D. Marty-Dessus) and SFU. We gratefully acknowledge B. van Wyk de Vries (LMV), J. Clague, G.W. Jones (SFU), K. Russell (UBC) and P. Friele, for fieldtrip assistance. Laboratory analyses have been funded by Volcanology laboratory and CNRS in LMV (R. Paris and V. Cayol). J.L. Devidal, C. Constantin and J-M. Hennot (LMV) are thanked for their expertise in making the thin sections and for SEM assistance, J. Cellier and R. Thirouard for XRD analyses (UCA-PARTNER-DRX in Clermont), J. Clague and F. van Wyk de Vries for editing the English writing. We acknowledge two anonymous reviewers and the Chief Editor Dr. Jose Luis Macias for the constructive comments and suggestions that have improved the manuscript.

References

The corrections made in this section will be reviewed and approved by a journal production editor. The newly added/removed references and its citations will be reordered and rearranged by the production team.

Andrews, G.D., Russell, J.K., Stewart, M.L., 2014. The history and dynamics of a welded pyroclastic dam and its failure. Bull. Volcanol. 76, 811.

Anthony, J.L., Marone, C., 2005. Influence of particle characteristics on granular friction. J. Geophys. Res. 110, B08409.

Bernard, B., 2008. Etude des Dépôts D'avalanches de Débris Volcaniques: Analyse Sédimentologique D'exemples Naturels et Identification des Mécanismes de Mise en Place Ph.D. Thesis. Univ. Blaise Pascal Clermont-Ferrand, France (in French).

K. Bernard. Quelques aspects sédimentaires des avalanches de débris volcaniques. Ph.D. Thesis Univ. Clermont-AuvergneFrance, 2015. (Unpub., in French). Available at: <NNT: 2015CLF22624>.<tel-01330779>.

~~Bernard, K., Thouret J-C., van Wyk de Vries, B., 2017. Emplacement and transformations of volcanic debris avalanches - A case study at El Misti volcano, Peru. J. Volcanol. Geotherm. Res. 340, 68-91.~~Bernard, K., Thouret, J-C., van Wyk de Vries, B., 2017. Emplacement and transformations of volcanic debris avalanches - a case study at El Misti volcano, Peru. J. Volcanol. Geotherm. Res. 340, 68–91.

Bernard, K., van Wyk de Vries, B., 2017. Volcanic avalanche fault zone with pseudotachylite and gouge in French Massif Central. J. Volcanol. Geotherm. Res. 347, 112–135.

Bernard, K., van Wyk de Vries, B., Thouret, ~~J-C.~~J.-C., 2019. ~~Fault textures in volcanic debris-avalanche deposits and transformations into lahars: The Pichu Pichu thrust lobes in south Peru compared to worldwide avalanche deposits~~Fault textures in volcanic debris-avalanche deposits and transformations into lahars: the Pichu Pichu thrust lobes in south Peru compared to worldwide avalanche deposits. J. Volcanol. Geotherm. Res. 371, 116–136.

Bestmann, M., Pennacchioni, G., Frank, G., Göken, M., 2011. Pseudotachylyte in muscovite-bearing quartzite: coseismic friction-induced melting and plastic deformation of quartz. J. Struct. Geol. 33, 169–186.

Bezeava, N.S., Swanson-Hyssell, N.L., Tikoo, S.M., Badyukov, D.D., Kars, M., Egli, R., Chareev, D.A., Fairchild, L.M., Khakhalov, E., Strauss, B.E., Lindquist, A.K., 2016. The effects of 10 to >160 GPa shock on the magnetic properties of basalt and diabase. Geochem. Geophys. Geosyst. 17, 4753–4771.

Blott, S.J., Pye, K., 2008. Particle shape: a review and new methods of characterization and classification. Sedimentology 55, 31–63.

Blundy, J., Cashman, K.V., 2005. Rapid decompression-driven crystallization recorded by melt inclusions from Mount St. Helens volcano. Geology 33, 793–796.

Caballero, L., Capra, L., 2011. ~~Textural analysis of particles from El Zaguán debris avalanche deposit, Nevado de Toluca volcano, Mexico: Evidence of flow behavior during emplacement~~Textural analysis of particles from El Zaguán debris avalanche deposit, Nevado de Toluca volcano, Mexico: evidence of flow behavior during emplacement. J. Volcanol. Geotherm. Res. 200, 75–82.

Capra, ~~L~~L., 2007. Volcanic natural dams: identification, stability, and secondary effects. Nat. Hazards 43, 45–61.

Capra, L., Macías, J.L., 2002. ~~The Cohesive Naranjo Debris-Flow Deposit (10 km3): A dam breakout flow derived from the Pleistocene Debris-Avalanche Deposit of Nevado de Colima Volcano (Mexico)~~The Cohesive Naranjo Debris-Flow Deposit (10 km3): a dam breakout flow derived from the Pleistocene Debris-Avalanche Deposit of Nevado de Colima Volcano (Mexico). J. Volcanol. Geotherm. Res. 117, 213–235.

Cashman, K.V., Thornber, C.R., Pallister, J.S., 2008. ~~From dome to dust: Shallow crystallization and fragmentation of conduit magma during the 2004-2006 dome extrusion of Mount St. Helens, Washington~~From dome to dust: Shallow crystallization and fragmentation of conduit magma during the 2004–2006 dome extrusion of Mount St. Helens, Washington. In: Sherrod, D.R. (Ed.), et al., ~~A volcano rekindled: The renewederuption of Mount St. Helens, 2004-2006. U.S. Geol. Surv. Prof. Pap~~A Volcano Rekindled: The Renewederuption of Mount St. Helens, 2004–2006. U.S. Geol. Surv. Prof. Pap, ~~1750~~vol. 1750. pp. 387–413.

Clague, J.J., Evans, S.G., Rampton, V.N., Woodsworth, G.J., 1995. Improved age estimates for the White River and Bridge River tephras, Western Canada. Can. J. Earth Sci. 32, 1172–1179.

Collins, G.S., Melosh, H.J., 2003. ~~Acoustic fluidization and the Extraordinary mobility of sturzstroms~~Acoustic fluidization and the extraordinary mobility of sturzstroms. J. Geophys. Res. 108, B102473.

Crawford, E., Mortensen, K., 2009. An Image J plugin for the rapid morphological characterization of separated particle sand an initial application to placergold analysis. Comput. Geosci. 35, 347–359.

Davies, T.R., McSaveney, M.J., 1999. Runout of dry granular avalanches. Can. Geotech. J. 36, 313–320.

Evans, D.G., Raffensperger, J.P., 1992. On the stream function for variable-density groundwater flow. Water Resour. Res. 28, 2141–2145.

Farquharson, J.I., Heap, M.J., Lavallée, Y., Varley, ~~N. R.~~N.R., Baud, P., 2016. Evidence for the development of permeability anisotropy in lava domes and volcanic conduits. J. Volcanol. Geotherm. Res. 323, 163–185.

Ferré, E.C., Zechmeister, M.S., Geissman, J.W., MathanaSekaran, N., Kocak, K., 2005. The origin of high magnetic remanence in fault pseudotachylites: theoretical considerations and implication for coseismic electrical currents. Tectonophysics 402, 125–139.

Folk, R.L., Ward, W.C., 1957. Brazos River bar: a study in the significance of grain size parameters. J. Sediment. Petrol. 27, 3–26.

Friele, P.A., Clague, J.J., 2004. Large Holocene land-slides from Pylon Peak, southwestern British Columbia. Can. J. Earth Sci. 41, 165–182.

Friele, P.A., Clague, J.J., Simpson, K., Stasiuk, M., 2005. Impact of Quaternary volcano on Holocene sedimentation in Lillooet River valley, British Columbia. Sediment. Geol. 176, 305–322.

Friele, P.A., Jakob, M., Clague, J.J., 2008. Hazard and risk from large landslide from Mount Meager volcano, British Columbia, Canada. ~~Georisk: Assess. Manage. Risk Eng. Sys. Geohazards~~Georisk: Assess. Manage. Risk Eng. Sys. Geohazard. 2, 48–64.

G1icken, H., 1986. ~~Rockslide-debris avalanche of May 18, 1980, Mount Saint Helens Volcano~~Rockslide-Debris Avalanche of May 18, 1980, Mount Saint Helens Volcano. Univ. Calif. Santa Barbara, Washington Ph. D. Thesis.

Goral, A., Litynska-Dobrzynska, I., Zorawski, W., Berent, K., Wojewoda-Budka, J., 2013. Microstructure of Al_2O_3-13TiO_2 coating deposited from nanoparticles by plasma spraying. ~~Archives of Metallurgy and Materials~~Arch. Metall. Mater. 58, 335–339.

Guthrie, R.H., Friele, P., Allstadt, K., Roberts, N., Evans, S.G., Delaney, K.B., Roche, D., Clague, J.J., Jakob, M., 2012. The 6 Augusts 2010 Mount Meager rock slide-debris flow, Coast Mountains, British Columbia: characteristics, dynamics, and implications for hazard and risk assessment. Nat. Hazards Earth Syst. Sci. 12, 1277–1294.

Heap, ~~M. J.~~M.J., Kolzenburg, S., Russell, ~~J. K.~~J.K., Campbell, ~~M. E.~~M.E., Welles, J., Farquharson, ~~J. I.~~J.I., Ryan, A., 2014. Conditions and timescales for welding block-and-ash flow deposits. J. Volcanol. Geotherm. Res. 289, 202–209.

Heap, M.J., Kennedy, B.M., Farquharson, J.I., Ashworth, J., Mayer, K., Letham-Brake, M., Reuschlé, T., Gilg, H.A., Scheu, B., Lavallée, Y., Siratovich, P., Cole, J., Jolly, A.D., Baud, P., Dingwell, D.B., 2017. A multidisciplinary approach to quantify the permeability of the Whakaari/ White Island volcanic hydrothermal system (Taupo Volcanic Zone, New Zealand). J. Volcanol. Geotherm. Res. 332, 88–108.

Heap, M.J., Gravley, D.M., Kennedy, B.M., Gilg, H.A., Bertolett, E., Barker, S.L., 2020. ~~Quantifying the role of hydrothermal alteration in creating geothermal and epithermal mineral resources: The Ohakuri ignimbrite (Taupō Volcanic Zone, New Zealand)~~Quantifying the role of hydrothermal alteration in creating geothermal and epithermal mineral resources: the Ohakuri ignimbrite (Taupō Volcanic Zone, New Zealand). J. Volcanol. Geotherm. Res. 390, 106703.

Hickson, C.J., Russell, J.K., Stasiuk, M.V., 1999. Volcanology of the 2350 B.P. Eruption of Mount Meager Volcanic Complex, British Columbia, Canada: implications for Hazards from Eruptions in Topographically Complex Terrain. Bull. Volcanol. 60, 489–507.

Hungr, ~~O~~O., 1995. A model for the runout analysis of rapid flow slides, debris flows, and avalanches. Can. Geotech. J. 32, 610–623.

Hungr, O., Evans, S.G., 1996. Rock avalanche runout prediction using a dynamic model. In: Senneset (Ed.), Landslides. Balkema, p. 1996 ~~ISBN 90 5410 8185~~(ISBN 90 5410 8185).

Hungr, O., Evans, S.G., 2004. Entrainment of debris in rock avalanches: an analysis of a long run-out mechanism. Geol. Soc. Am. Bull. 116, 1240–1252.

Ingebritsen, S.E., Geiger, S., Hurwitz, S., Driesner, T., 2010. Modeling magmatic hydrothermal systems. Rev. Geophys. 48, 1–33.

John, D.A., Sisson, T.W., Breit, G.N., Rye, R.O., Vallance, J.W., 2008. Characteristics, extent and origin of hydrothermal alteration at Mount Rainier Volcano, Cascades Arc, USA: implications for debris-flow hazards and mineral deposits. J. Volcanol. Geotherm. Res. 175, 289–314.

Jordan, P., 1994. ~~Debris flow in the southern Coast Mountains, British Columbia: Dynamic behaviour and physical properties~~Debris Flow in the Southern Coast Mountains, British Columbia: Dynamic Behaviour and Physical Properties Ph.D. Thesis. Univ. British Columbia, Vancouver, p. 272.

Kaproth, ~~B. M.~~B.M., Marone, C., 2014. Evolution of elastic wave speed during shear-induced damage and healing within laboratory fault zones. J. Geophys. Res. Solid Earth 119, 4821–4840.

Keigler, R., Thouret, ~~J-C.~~J.-C., Hodgson, K.A., Neal, V.E., Lecointre, J.A., Procter, J.N., Cronin, S.J., 2011. The Whangaehu Formation: Debris-avalanche and lahar deposits from ancestral Ruapehu volcano, New Zealand. Geomorphology 133, 57–79.

Kokelaar, B.P., Graham, ~~R. L.~~R.L., Gray, J.M.N.T., Vallance, J.W., 2014. Fine-grained linings of leveed channels facilitate runout of granular flows. Earth Planet. Sci. Lett. 385, 172–180.

Launeau, P., Robin, Y.F., 1996. Fabric analysis using the intercept method. Tectonophysics 267, 91–119.

Lavallee, Y., Mitchell, T.M., Heap, J., Vasseur, J., Hess, ~~K-U.~~K.-U., Hirose, T., Dingwell, D.B., 2012. Experimental generation of volcanic pseudotachylytes: constraining rheology. J. Struct. Geol. 38, 222–233.

Lavallee, Y., Hirose, T., Kendrick, J.U., Hess, K.U., Dingwell, D.B., 2015. Fault rheology beyond frictional melting. ~~Proc. Natl. Acad. Sci. USA~~Proc. Natl. Acad. Sci. U. S. A. 112, 9276–9280.

Legros, ~~J-F.~~J.-F., Cantagrel, ~~J-M.~~J.-M., Devouard, B., 2000. Pseudotachylite (Frictionite) at the base of the Arequipa Volcanic landslide (Peru): implications for emplacement mechanisms. J. Geol. 108, 601–611.

Mackaman-Lofland, C., Brittany, D.B., Taddeucci, J., Wohletz, K., 2014. ~~Sequential fragmentation/transport theory, pyroclast size-density relationships, and the emplacement dynamics of pyroclastic density currents – A case study on the Mt. St. Helens (USA) 1980 eruption~~Sequential fragmentation/transport theory, pyroclast size-density relationships, and the emplacement dynamics of pyroclastic density currents – a case study on the Mt. St. Helens (USA) 1980 eruption. J. Volcanol. Geotherm. Res. 275, 1–13 Available at. http://works.bepress.com/brittany_brand/11.

Magloughlin, J.F., 2005. ~~Immiscible sulfide droplets in pseudotachylyte: Evidence for high temperature (>1200 °C) melts~~Immiscible sulfide droplets in pseudotachylyte: evidence for high temperature (>1200 °C) melts. Tectonophysics 402, 81–91.

Major, J.J., Voight, B., 1986. Sedimentology and clast orientations of the 18 May 1980 southwest flank lahars, Mount St. Helens, Washington. ~~J. Sed. Petrology~~J. Sed. Petrol. 56, 691–705.

Major, J.J., Janda, R.J., Daag, A.S., 1995. Watershed disturbance and lahars on the east side of Mount Pinatubo during the mid-June 1991 eruptions. In: Newhall, C.G., Punongbayan, R.S. (Eds.), Fire and Mud, Eruptions and Lahars of Mount Pinatubo, Philippines. Washington Press, New-York, pp. 895–919.

McKinnon, M., 2008. Dynamic analyses of Canadian landslides. In: Loca, J., Perret, D., Turmel, D., Demers, D., Lerouel, S. (Eds.), Comptes Rendus de la 4è Conférence Canadienne sur les Géorisques: Des Causes à la Gestion. Laval Univ. Press, Quebec, p. 594.

McSaveney, M.J., 1978. Sherman Glacier rock avalanche. In: Voight, B. (Ed.), ~~Rockslides and avalanches, 1: Natural phenomena~~Rockslides and Avalanches, 1: Natural Phenomena. Elsevier, Amsterdam, pp. 197–258.

Mehl, K.W., Schmincke, H.-U., 1999. Structure and emplacement of the Pliocene Roque Nublo debris avalanche deposit, Gran Canaria, Spain. J. Volcanol. Geotherm. Res. 94, 105–134.

Michol, K.A., Russell, J.K., Andrews, G.D.M., 2008. Welded block and ash flow deposits from Mount Meager, British Columbia, Canada. J. Volcanol. Geotherm. Res. 169, 121–144.

Mueller, S.B., Kueppers, U., Huber, B.S., Hess, ~~K.-U.~~K.-U., Poesges, G., Ruthensteiner, B., Dingwell, D.B., 2018. Aggregation in particle rich environments: a textural study of examples from volcanic eruptions, meteorite impacts, and fluidized bed processing. Bull. Volcanol. 80, 32.

Palmer, B.A., Neall, V.E., 1991. Contrasting lithofacies architecture in ring-plain deposits related to edifice construction and destruction, the Quaternary Stratford and Opunake Formations, Egmont Volcano, New Zealand. Sediment. Geol. 74, 71–88.

Pierson, T.C., Scott, K.M., 1985. Downstream dilution of a lahar: transition from debris flow to hyperconcentrated-flow. Water Resour. Res. 21, 1511–1524.

Read, P.B., 1977. Meager Creek volcanic complex, southwestern British Columbia. In: Current Research, Part A: Geol. Surv. Can. Pap, ~~77-1A~~vols. 77-1A. pp. 277–281.

Read, P.B., 1979. Geology, Meager Creek geothermal area, British Columbia: Geological Survey of Canada Open File, 603, 1 sheet, scale 1:20 000.

Reid, M.E., Sisson, T.W., Brien, D.L., 2001. Volcano collapse promoted by hydrothermal alteration and edifice shape, Mount Rainier, Washington. Geology 29, 779–782.

Reznick, B., Kontny, A., Fritz, J., Gerhards, U., 2016. Shock-induced deformation phenomena in magnetite and their consequences on magnetic properties. Geochem. Geophys. Geosyst. 17, 2374–2393.

Roberti, G., 2019. Mount Meager, a glaciated volcano in a changing cryosphere: hazards and risk challenges. In: Earth Sciences. Univ. Clermont-Auvergne, 2018. English. NNT: 2018CLFAC040. Tel-02010551.

Roberti, G., Friele, P., van Wyk de Vries, B., Ward, B., Clague, J.J., Perotti, L., Giardino, M., 2017. Rheological evolution of the Mount Meager 2010 debris avalanche, southwestern British Columbia. Geosphere 13, 369–390.

Russell, J.K., Hickson, C.J., Andrews, G., 2007. Canadian Cascade volcanism: subglacial to explosive eruptions along the Sea to Sky Corridor, British Columbia. In: Stelling, P., Tucker, D.S. (Eds.), Floods, Faults, and Fire: Geological Field Trips in Washington State and Southwest British Columbia. G.S.A. Field Guide, Floods, Faults, and Fire. Stelling, P., Tucker, D.S, ~~9~~vol. 9. Geol. Soc. Am, pp. 1–29.

Scott, K.M., Vallance, J.W., Pringle, P.T., 1995. Sedimentology, behavior, and hazards of debris flows at Mount Rainier, Washington. In: U.S. Geol. Surv. Prof. Pap, ~~1547~~vol. 1547. p. 56.

Scott, K.M., Vallance, J.W., Kerle, N.J., Macias, L., Strauch, W., Devoli, G., 2005. Catastrophic precipitation-triggered lahar at Casita volcano, Nicaragua: Occurrence, bulking and transformation. ~~Earth Surf. Process. Landforms~~Earth Surf. Process. Landf. 30, 59–79.

Simpson, K.A., Stasiuk, M., Shimamura, K., Clague, J.J., Friele, P., 2006. Evidence for catastrophic volcanic debris flows in Pemberton Valley, British Columbia. Can. J. Earth Sci. 43, 679–689.

Spray, J.G., 1992. A physical basis for the frictional melting of some rock-forming minerals. Tectonophysics 204, 205–221.

Spray, ~~J. G.~~J.G., 1997. Superfaults. Geology 25, 579–582.

Spray, J.G., 1999. Shocking rocks by cavitation and bubble implosion. Geology 27, 695–698.

Spray, J.G., 1999. Pseudotachylite controversy: Fact or friction?. Geology 23, 1119–1122.

Suzuki-Kamata, K., Kusano, T., Yamasaki, K., 2009. Fractal analysis of the fracture strength of lava dome material based on the grain size distribution of block-and-ash flow deposits at Unze volcano, Japan. ~~Sedim. Geol.~~Sediment. Geol. 220, 162–168.

Taddeucci, J., Palladino, D.M., 2002. Particle size-density relationships in pyroclastic deposits: inferences for emplacement processes. Bull. Volcanol. 64, 273–284.

Trepmann, C., Stöckhert, B., 2003. Quartz microstructures developed during non-steady state plastic flow at rapidly decaying stress and strain rate. J. Struct. Geol. 25, 2035–2051.

Turner, M.B., Cronin, S.J., Stewartd, R.B., Bebbington, M., Smith, I.E.M., 2008. Using titanomagnetite textures to elucidate volcanic eruption histories. Geology 36, 31–34.

Vallance, J.W., Scott, K.M., 1997. The Osceola Mudflow from Mount Rainier: sedimentology and hazard implications of a huge clay-rich debris flow. Geol. Soc. Am. Bull. 109, 143–163.

Waythomas, C.F., Miller, T.P., Beget, J.E., 2000. Record of Late Holocene debris avalanches and lahars at Iliamna Volcano, Alaska. J. Volcanol. Geotherm. Res. 104, 97–130.

Weidinger, J.T., Koruo, O., Munack, H., Altenberger, U., Dunning, S.A., Tippelt, G., Lottermoser, W., 2014. Giant rockslides from the inside. Earth Planet. Sci. Lett. 389, 62–73.

Wohletz, K.H., Sheridan, M.F., Brown, W.K., 1989. ~~Particle Size Distribution and the sequential fragmentation/transport theory applied to volcanic~~

Highlights

- Sedimentological parameters help to distinguish the Meager different lithofacies.
- Coating matrix, fluidized disaggregation change the initial polymodal distribution.
- We describe the pseudotachylitic clast coating in impact melt breccias.
- We correlate sequential coating to epithermal fault and temperature pressure regime.
- We identify how the proximal avalanche transformed into a highly mobile debris flow.

We observe a brown clayey matrix (1), which is overlain unconformably (T1–2 in Fig. 1B) by a cataclastic, grey rhyodacite lithofacies (2) and a matrix-rich lithofacies (3, Fig. 1B) showing sub-rounded rhyodacite blocks. A semi-quantitative description of deposits is established using a SPO analysis of the 1157 clasts and the software ImageJ (see *Supplemental File 1*). The clast/matrix values are between 0.54 in MB and 1.09 in DC with a mean value around ~0.93. The mixed debris in MB is associated with a polymodal clast-size distribution, with a/b = 1.35 and ellipse = 3.87 (SPO from 51 clasts, Table 1). We differentiate the cataclastic, grey rhyodacite lithofacies (2) in downstream of the Capricorn-Meager confluence (Fig. 2A). The flow breccias are extruded and tilted northward. Cataclastic lava breccias are tilted in semi-horsts and matrix mixture in graben in downstream of frontal thrust (Fig. 2B). Jigsaw fractures are observed in the cataclastic rhyodacite breccias in semi-horsts (Fig. 2B). The grabens are filled by a brown clayey matrix (1) overlain by a mixed matrix (3 in Fig. 1, Table 1). The clast-size distribution is unimodal with mean values around a/b = 1.13 and ellipse = 15.2 (SPO from 193 clasts, see *Supplemental File 1*). Along the extensional faults, the rhyodacite breccias are tilted and sheared (Fig. 2B). At the confluence, the frontal deposits have been back-thrust (Fig. 2C). Cataclastic lava breccias in semi-horst and matrix mixture are thrust with unconformity contacts at the front lobe (Fig. 2C–D). These are tilted and abraded along sheared contact. The thin discontinuous lithofacies are sheared along the inverted extensional faults. The thrust lobe (Fig. 2) is characterized by a series of thrust units at the front. The avalanche lithofacies assemblage becomes thicker along serial thrust contacts (Fig. 2D–E). A unimodal clast-size distribution characterizes the matrix deposits with mean values around a/b = 1.08 and ellipse = 8.32 (SPO from 749 clasts, see *Supplemental File 1*). Underlying, water saturated lithofacies (Figs. 2C and 3C–D, Table 1) are extruded along reverse faults. Debris-flow deposits and hybrid avalanche deposits are differentiated at the front of the thrust lobe. Locally, reworked alluvial pebbles are observed. The dam-breach flood has contributed to the polymodal clast-size distribution (SPO from 164 clasts) of the hybrid avalanche deposits with mean values around a/b = 1.08 and ellipse = 12.08. Clastic gradation of sedimentary lithofacies assemblage with reverse grading is correlated with deposit morphology (Figs. 1 and 2).

A similar grain-size distribution of the sandy-gravel matrix and the power regression between matrix percent and matrix/gravels (Eq. (1) with R^2 = 0.98 in Figs. 5A and 14A) implicate a similar cataclastic origin with a co-genetic evolution of lithofacies. These values of the sandy-gravel matrix are close to those of the sandy layer before the impact-sheared contact along avalanche fault zone in French Massif Central (Bernard and van Wyk de Vries, 2017). The increasing D-values related to the percentage of matrix (MB, DC) and matrix-gravel ratio are related to jigsaw fit-textures (<10.3% matrix), and the primary fracturing (~41% matrix, MB-TS) with 40 to 50% *syn*-emplacement breccias along the downstream thrust lobe (TS and DC, Fig. 14A). The matrix percent *vs*. matrix/gravels diagram helps to distinguish primary fracturing from thermal effect such as melt-corroded clast around ~61% (bx2 units, Hickson et al., 1999), dilation and shear fracturing with 22% matrix, close to the Tutupaca lava breccias in Peru (Bernard, 2015). The secondary fracturing between 73 and 79% matrix is related to the hydromagmatic fragmentation of the polymodal hybrid deposits (γ = −0.4 + 0.4 in DC, σ ~ 2.43, Wohletz et al., 1989), showing coating matrix with secondary bands and microfractures (Fig. 10). The parent volcanic processes include the pyroclastic domain (γ = −0.5–0.97, Vulsinni, Taddeucci and Palladino, 2002; γ = −0.8–0.2, Mount Saint Helens, Mackaman-Lofland et al., 2014) for 57% of the granular fractions around −1.6 Φ (Figs. 5–6, *Supplemental file 1*). The avalanche deposits in Peru and Canada present similar γ-values between −0.1 + 0.2 (Bernard, 2015). We differentiate the avalanche deposits in subduction zones. These deposits appear between the reworked Pardines deposits in French Massif Central (Kg = 1, SKg = 0.1-0.2) and Tutupaca avalanche deposits in Peru (Md = 3-2 Φ, σ = 1.25), in accordance with energy fragmentation/energy potential *vs*. D values (Bernard et al., 2019).

The following is the supplementary data related to this article.

Multimedia Component 1

Supplemental File 1

Textural variations of lithofacies as deduced from SPO analysis. A. The polymodal mixed debris in MB with a/b = 1.35 and ellipse = 3.87 (SPO from 51 clasts); B. An unimodal clayey matrix in graben (TS, SPO from 193 clasts) with a/b = 1.13 and ellipse = 15.2; C. An unimodal clast-size distribution of the matrix lithofacies in PL with a/b = 1.08 and ellipse = 8.32 (SPO from 749 clasts); D. A polymodal clast-size distribution of the hybrid avalanche deposits in DC with a/b = 1.08 and ellipse = 12.08 (SPO from 164 clasts).

alt-text: Supplemental File 1

Queries and Answers

Query: Your article is registered as a regular item and is being processed for inclusion in a regular issue of the journal. If this is NOT correct and your article belongs to a Special Issue/Collection please contact m.ayyamperumal@elsevier.com immediately prior to returning your corrections.
Answer: Yes

Query: We find that the input provided for the credit roles is in incorrect format. Also ensure that the roles are as defined in the following list. For any roles not listed in the following, we will not be able to process: Conceptualization; Data curation; Formal analysis; Funding acquisition; Investigation; Methodology; Project administration; Resources; Software; Supervision; Validation; Visualization; Writing - original draft; Writing - review & editing.

Answer: The fieldwork in Canada trip has been funded by the French ambassador (D. Marty-Dessus) and SFU. We gratefully acknowledge B. van Wyk de Vries (LMV), J. Clague, G.W. Jones (SFU), K. Russel (UBC) and P. Friele, for fieldtrip assistance. Laboratory analyses have been funded by Volcanology laboratory and CNRS in LMV (R. Paris and V. Cayol). J.L. Devidal, C. Constantin and J-M. Hennot (LMV) are thanked for their expertise in making the thin sections and for SEM assistance, J. Cellier and R. Thirouard for XRD analyses (UCA-PARTNER-DRX in Clermont), J. Clague and F. van Wyk de Vries for editing the English writing. We acknowledge two anonymous reviewers and the Chief Editor Dr. Jose Luis Macias for the constructive comments and suggestions that have improved the manuscript.

Query: Please confirm that given names and surnames have been identified correctly and are presented in the desired order, and please carefully verify the spelling of all authors' names.
Answer: Yes

Query: The author names have been tagged as given names and surnames (surnames are highlighted in teal color). Please confirm if they have been identified correctly.
Answer: Yes

Query: Citation "Graham et al., 2014" has not been found in the reference list. Please supply full details for this reference.
Answer: I would remove the reference "Graham et al., 2014"

Query: Please check the layout and presentation of Tables if correct.
Answer: Yes

Query: Citation "Bernard et al., 2017" has not been found in the reference list. Please supply full details for this reference.
Answer: The citation "Bernard et al., 2017" is related to the following reference:
Bernard, K., Thouret J-C., van Wyk de Vries, B., 2017. Emplacement and transformations of volcanic debris avalanches - A case study at El Misti volcano, Peru. J. Volcanol. Geotherm. Res. 340, 68-91.

Query: Uncited reference: This section comprises references that occur in the reference list but not in the body of the text. Please position each reference in the text or, alternatively, delete it. Thank you.
Answer: I would move the reference "Bernard and Thouret 2017". SPO analysis is related to the following references (Launeau and Robin, 1996; Bernard, 2015).
Supplemental File 1: Textural variations of lithofacies as deduced from SPO analysis (Launeau and Robin, 1996; Bernard, 2015). A. The polymodal mixed debris in MB with *a/b* = 1.35 and ellipse = 3.87 (SPO from 51 clasts); B. An unimodal clayey matrix in graben (TS, SPO from 193 clasts) with *a/b* = 1.13 and ellipse = 15.2; C. An unimodal clast-size distribution of the matrix lithofacies in PL with *a/b* = 1.08 and ellipse = 8.32 (SPO from 749 clasts); D. A polymodal clast-size distribution of the hybrid avalanche deposits in DC with *a/b* = 1.08 and ellipse = 12.08 (SPO from 164 clasts).

Query: Correctly acknowledging the primary funders and grant IDs of your research is important to ensure compliance with funder policies. We could not find any acknowledgement of funding sources in your text. Is this correct?
Answer: Yes